



1

N 64 32352
(ACCESSION NUMBER)

87
(PAGES)

CR54195
(NASA CR OR TMX OR AD NUMBER)

(THRU)

(CODE)

17
(CATEGORY)

FIRST QUARTERLY REPORT

LUBRICATION ANALYSIS IN TURBULENT REGIME

by

F.K. Orcutt, C.W. Ng, J.H. Vohr, and E.B. Arwas

prepared for

NATIONAL AERONAUTICS AND SPACE ADMINISTRATION

CONTRACT NASw-1021

OTS PRICE

XEROX \$ 3.00 per

MICROFILM \$.25 per

MTI
MECHANICAL TECHNOLOGY INCORPORATED
MTI
research - development - manufacturing

NOTICE

This report was prepared as an account of Government sponsored work. Neither the United States, nor the National Aeronautics and Space Administration (NASA), nor any person acting on behalf of NASA:

- A) Makes any warranty or representation, expressed or implied, with respect to the accuracy, completeness, or usefulness of the information contained in this report, or that the use of any information, apparatus, method, or process disclosed in this report may not infringe privately owned rights; or
- B) Assumes any liabilities with respect to the use of, or for damages resulting from the use of any information, apparatus, method or process disclosed in this report.

As used above, "person acting on behalf of NASA" includes any employee or contractor of NASA, or employee of such contractor, to the extent that such employee or contractor of NASA, or employee of such contractor prepares, disseminates, or provides access to, any information pursuant to his employment or contract with NASA, or his employment with such contractor.

Requests for copies of this report should be referred to:

National Aeronautics and Space Administration
Office of Scientific and Technical Information
Attention: AFSS-A
Washington, D.C. 20546

CASE FILE COPY

FIRST QUARTERLY REPORT

LUBRICATION ANALYSIS IN TURBULENT REGIME

by

F. K. Orcutt, C. W. Ng, J. H. Vohr and E. B. Arwas

prepared for

NATIONAL AERONAUTICS AND SPACE ADMINISTRATION

October 1, 1964

CONTRACT NASw-1021

Technical Management
NASA Lewis Research Center
Cleveland, Ohio
Space Electric Power Office
Joseph P. Joyce
Robert T. Wainwright

MECHANICAL TECHNOLOGY INCORPORATED
968 Albany-Shaker Road
Latham, New York

TABLE OF CONTENTS

	Page
SUMMARY	1
INTRODUCTION	2
REVIEW OF PREVIOUS STUDIES	4
PLAN OF RESEARCH	6
GEOMETRICAL PARAMETERS OF TILTING-PAD BEARINGS	8
Pivot Location	8
Pad Mass and Inertia	9
Geometrical Preload Coefficient	9
Test Bearing Design	11
THEORETICAL ANALYSIS OF THE TILTING-PAD BEARING IN THE TURBULENT FLOW REGIME	13
Linearized Turbulent Lubrication Theory for a Partial-Arc Bearing ..	13
Dynamic Load Analysis of the Partial-Arc Bearing	14
Dynamic Analysis of the Tilting Pad	15
Analysis of the Composite Tilting-Pad Bearing	16
Calculated Static and Dynamic Characteristics for the Tilting-Pad Bearing	17
DYNAMIC LOAD JOURNAL BEARING APPARATUS	19
Mechanical Components	19
Instrumentation	20
PRELIMINARY EXPERIMENTS	22
FLOW STABILITY EXPERIMENTS	24
Use of Electrochemiluminescent Flow Visualization Technique for the Study of Flow Patterns in a Glass Journal with Close Clearances	24
Torque Measurements to Determine Flow Instabilities Between Eccentric Cylinders with Close Clearance	25
Visual Study of Flow Stability in Partial-Arc Bearing Configuration	26

TABLE OF CONTENTS, cont.

	Page
FUTURE WORK -----	27
REFERENCES -----	28
NOMENCLATURE FOR MAIN TEXT -----	29
APPENDICES -----	30
A - NUMERICAL ANALYSIS FOR LINEARIZED, TURBULENT, INCOMPRESSIBLE, FULL AND PARTIAL JOURNAL BEARINGS -----	A-1
B - DYNAMIC LOAD ANALYSIS OF THE TILTING-PAD BEARING -----	B-1
FIGURES	

SUMMARY

32352

A turbulent-flow lubrication theory for the composite tilting-pad bearing has been developed. Design data calculations have been made and results are presented in this report. The theoretical static load capacity, dynamic load properties, frictional torque and flow are given for a wide range of conditions covering the practical operating range for a four-pad, 80 degree pad, arc bearing.

Modifications to the dynamic load bearing apparatus, including the installation of a torquemeter for measurement of test bearing frictional torque, have been made. Preliminary experiments to determine the parasitic torque characteristics of the apparatus have begun and initial results are given. The tilting-pad test bearing has been designed and fabrication is underway.

Plans have been made for continuation of the studies of the fundamentals of superlaminar flow in the film between a rotating inner cylinder and an eccentric outer surface which may be a full or partial-arc cylinder. Preparations for preliminary experiments using a new technique for flow visualization, electrochemiluminescence, have begun.

Author

INTRODUCTION

Superlaminar flow of the lubricant film in journal bearings may occur in high-speed rotating machinery using low kinematic viscosity fluids as the bearing lubricant. Dynamic space power turbo-machinery in which the liquid metal working fluid is used as the bearing lubricant are an example of this type of rotating machinery.

The performance of a bearing will change significantly as the lubricant film flow becomes superlaminar and the difference, as compared to laminar flow behavior, will become greater as the Reynolds' number is increased. The gross effects of flow transition on performance with unidirectional load are to increase the friction power loss, the load-carrying capacity and the shaft attitude angle for a given eccentricity. Considering only the effects on static load performance, it appears that superlaminar flow results in improved bearing performance. However, there are other considerations which are usually much more important in high-speed rotating machinery. The principal loads on the bearings of such machines are dynamic loads resulting from rotor unbalance or from external sources. Moreover, it is the dynamic load characteristics of the bearings of a rotor-bearing system which help determine the critical speeds and the threshold of instability of the rotor-bearing system. Another major consideration — especially in compact, high-performance machinery — is power loss in the bearings. Frictional power loss in the bearing rises sharply with the transition to superlaminar flow. Power losses directly attributable to the bearings have represented a sizeable portion of the total power output of early, space power CRU's. These losses reduce the system efficiency and make it difficult to avoid serious thermal gradients in the region of the bearings and their supports.

It is apparent that the behavior of bearings operating in the superlaminar flow regime is quite different from that of conventional bearings in which the flow in the lubricant film is laminar. For rational design of rotor-bearing systems to be operated at high speed using low kinematic viscosity lubricants, it is necessary to have a verified lubrication theory for superlaminar flow that includes provision for computing the vital dynamic load properties of the bearing.

The broad objectives of this program, and of the program which preceded it, are to:

- (a) Contribute to the development of a comprehensive theory for lubrication in the superlaminar flow regime;
- (b) Apply the theory to generate the engineering data for practical bearing configuration in superlaminar regime;
- (c) Experimentally test the practical usefulness of the theory as a design tool and, while so doing, to supplement the theoretical results with experimental observations.

This report describes the work performed during the first three-month period of this program.

REVIEW OF PREVIOUS STUDIES

Before proceeding with a description of the work of the present program, it is appropriate to briefly review the results of the program which preceded this one. There were two principal areas of investigation in the program on turbulent-flow lubrication which was done at MTI under NASA sponsorship (Contract NASw-771). They were

- (a) Determination of static and dynamic properties of basic bearing geometries (plain circular and partial-arc) in the superlaminar flow regime.
- (b) Torque measurement and visual observation of flow between non-concentric cylinders extending to very high Reynolds numbers.

The partial-arc pad is the basic element or building block of most practical bearings for high-speed rotary machinery. Development of a useful theory for design analysis of practical, superlaminar flow bearing hinges on the existence of a verified theory for the individual partial-arc pad. For example, the performance of the tilting-pad bearing is governed by the static and dynamic characteristics of the individual pads which make up the complete bearing. During this program, the eddy viscosity-turbulent flow lubrication theory of Ng and Pan (Ref. 5) was extended to permit calculation of bearing dynamic properties. Calculations of both static and dynamic properties were made for a 100 degree arc bearing and were verified by experiment. Agreement was good between calculated and measured rotor response for a wide range of operating conditions for Reynolds numbers up to 13,300. ~~This is shown by the sample results taken from Reference 1 and given in Fig. 1.~~

The calculated bearing properties were used to compute the conditions for onset of fractional, frequency whirl of the shaft and these also compared closely with experimental measurements. Measured and calculated steady-state load capacities for the bearing were compared and found to be in excellent agreement. As a result of these studies, it was concluded that the eddy-viscosity turbulent flow lubrication theory for the partial arc had been shown to be sufficiently accurate to be of practical value in design calculations.

Superlaminar flow in journal bearings is complicated by the fact that there are two distinct modes, vortex flow and fully developed turbulence. The critical Reynolds number is different for each of these and, depending on the clearance ratio, either one can set in first. A fundamental study of these flow regimes in concentric and eccentric annuli, both with and without imposed axial pressure

gradient, was judged to be necessary in order to guide future development of a more comprehensive theory. This is true, particularly for vortex flow, since the formulation of the present theory is based on concepts for fully developed turbulent flow only.

The friction torques and flow regimes were studied through accurate torque measurements and visual studies of the flow regimes (Ref. 2). Transition speeds to vortex and turbulent flows were obtained as functions of eccentricity and the effect of axial pressures on these transition speeds was demonstrated. In addition, design charts for calculating journal bearing friction in superlaminar regime were obtained.

PLAN OF RESEARCH

In this program, the work of the previous program will be continued and extended in both a) the determination of the static and dynamic load properties of the particular bearing types that are judged to be most suitable for high-speed turbomachinery, where the bearing film is superlaminar, and b) in the investigation of the fundamental principles of flow in the bearing film for both vortex and fully-developed turbulence.

The theory and computational methods which were used and verified for single bearing elements will now be extended and applied to obtain design data for the multiple tilting-pad and the floating-ring journal bearings. The static and dynamic load characteristics and the frictional torque are to be calculated and verified experimentally for each bearing type and for a wide range of conditions. The tilting-pad and floating-ring bearings were chosen because, from both theoretical considerations and practical experience, they offer unique advantages for very high-speed rotary machinery applications. The tilting-pad bearing is generally recognized as having the best stability characteristics of any of the self-acting (hydrodynamic), journal bearing types. It can have very high load-carrying capacity. On the other hand, power loss is also quite high. The two lubricant films of the floating-ring bearing give it very high damping which results in good dynamic load and stability characteristics. A major advantage is substantially lower power loss since the shear rate and the Reynolds number of the inner film are lower than they are for an equivalent plain journal bearing because of ring rotation. Frictional resistance to shaft rotation comes only from the inner film, of course. Disadvantages include lower load-carrying capacity than most journal bearing types and possible difficulties in assuring that both hydrodynamic films are initiated when the shaft begins to rotate. We expect that this program will produce design data including some operating experience with a well-instrumented system for both of these bearing types covering both laminar and superlaminar flow regimes. This data should be directly applicable to such design decisions as choice of bearing type, specification of bearing design parameters, and determination of the effect of the bearing on system dynamics and power loss.

A principal objective of the bearing film-flow studies will be to investigate the effects of clearance between the cylinders and confirm the results which have been obtained with large clearance ratio at the much smaller clearances that are

representative of practical bearings. Very large clearances ($C/R \approx 0.1$ in/in.) were used in the previous experiments in order to obtain very high Reynolds' numbers at rotational speeds which could be achieved without elaborate, difficult-to-work-with equipment. In addition, large clearances were necessary to use the powdered aluminum tracer technique for flow visualization. In this program we hope to perform flow visualization experiments with considerably smaller clearances, although the range of Reynolds' numbers will be smaller, by developing a new technique for flow visualization which has not previously been applied to lubrication studies. Torque measurements will also be made for smaller clearance ratios in order to extend the empirical relationship of Wendt which has been used to take account of the effects of clearance ratio on frictional torque between rotating, concentric cylinders to the case of eccentric cylinders. Another area requiring investigation is the flow between a rotating inner cylinder and a partial-arc outer surface. Differences between the flow in this configuration and that between two complete cylinders are anticipated because of entrance effects at the leading edge of the arc. In the case of two cylinders, the same lubricant is constantly recycling around the clearance since it is an unending path. When the outer surface is an arc, there is a distinct beginning and end of the flow path and the effects on local flow of upstream flows, or the history of flow, will be different. There is some evidence of such differences now. The criterion for transition to superlaminar flow between eccentric cylinders which was developed by DiPrima (Ref. 3) was found to be surprisingly accurate for a partial-arc bearing (Ref. 4), but it was not nearly so accurate for the eccentric cylinders used in the previous program (Ref. 2). Because of these differences and because the partial arc is a basic bearing building block, studies of the flow in this configuration are needed.

GEOMETRICAL PARAMETERS OF TILTING PAD BEARINGS

The tilting-pad journal bearing consists of a set of pads which are individually pivoted, as shown schematically in Fig. 2. The geometrical parameters that define the bearings are:

- a) Bearing diameter (D)
- b) Number of pads
- c) Angular extent of the pads (β)
- d) Slenderness ratio ($\frac{L}{D}$)
- e) Pad clearance ratio ($\frac{C}{R}$)
- f) Pivot location ($\frac{\theta_P}{\beta}$)
- g) Pad mass and inertia
- h) Geometrical preload coefficient (m)

The parameters which are peculiar to this type of bearing are f, g and h, and these are discussed briefly below.

Pivot location

Each pad of the bearing is pivoted individually — generally by means of a rolling contact pivot. With proper design, the friction torque in the pivot is negligibly small in comparison with the moment induced in the fluid film when the resultant of the fluid film forces does not pass through the pivot. Each bearing pad will, therefore, assume an inclination such that the resultant of the fluid film forces passes through its pivot point. Thus, the location of the pivot point is critical since it governs the inclination that each pad will assume, hence the magnitude of the hydrodynamic pressures that are generated in the fluid film. Where the bearing has to be designed for either direction of rotation, a centrally located pivot ($\frac{\theta_P}{\beta} = .5$) is generally desirable.* Where the bearing is subject only to

* We are concerned here with journal bearing pads which are circular arcs. Such pads can generate hydrodynamic pressures, with centrally located pivots. The situation is quite different in the case of thrust bearings, where it can be shown that perfectly flat, centrally pivoted pads cannot generate hydrodynamic pressures. The load capacity exhibited by centrally pivoted, thrust bearing pads is almost entirely due to the fact that the pads "crown" under load, as a result of a) the distributed load on the active faces and the point (or line support) on the back faces of the pads, and b) the thermal gradients across the pads caused by heat generated by fluid shear on the active faces of the pads.

one direction of rotation, an increase in load-carrying capacity can be achieved by locating the pivot point a little after the mid-plane of the pads.

Pad Mass and Inertia

Proper functioning of tilting-pad bearings, under dynamic loads is predicated upon the pads being able to "track" the orbits of the journal. As the journal center moves along an orbit, the individual pads of the bearing must vary their inclinations, such that the vector sum of the fluid-film forces generated in the pads is always equal and opposite to the instantaneous journal load. If this condition is not satisfied, the tilting-pad bearing loses much of its advantage. It will approach in performance the fixed pad bearing and will become subject to a relatively low threshold of instability. The ability of the tilting-pad bearing to track journal motions can be analyzed in terms of the inertia of the individual pads and the stiffness and damping of their fluid films. The analysis yields equations which define: a) the magnification factor (i.e., the ratio of the amplitudes of motion of the pads to those of the journal), and b) the phase angle between these motions — in terms of the mass of the pads and the stiffness and damping coefficients of the fluid film. The value of the pad mass, at which the phase angle is 90° (compared to 0° if the pads have zero mass) is called the critical mass of the pads (M_{crit}). In order to assure satisfactory tracking of the journal orbits, the pads should be designed such that their mass is a small fraction of the critical mass. In practice, it is found that satisfactory tracking is achieved if the pad mass is less than one-half the critical pad mass. The critical pad mass has been computed and plotted, in the design charts included in this report, as a function of Sommerfeld Number and Reynolds' number, to facilitate design calculations.

Geometrical Preload Coefficient

Geometrical preloading is used in order to achieve:

- a) High bearing stiffness, even with zero net load on the shaft
- b) Positive fluid film pressures acting on all the bearing pads (even those located in the part of the bearing away from the direction of load).

Geometrical preloading is achieved by assembling the pads such that their centers of curvature, with zero inclinations, form a circle of radius "a" about the center of the bearing. Figures 3A and 3B show, respectively, the geometrical arrangement of the pads without and with geometrical preload.

Let:

$$\begin{aligned} R_P &= \text{Radius of curvature of the pads as machined} \\ R_S &= \text{Radius of shaft as machined} \\ a &= \text{Radius of preload circle} \\ C_P = R_P - R_S &= \text{Radial clearance of the pads (machined clearance)}. \end{aligned}$$

In the preload case, "the bearing radius" is now defined as:

$$R_B = R_P - a.$$

The "bearing radial clearance" (i.e., running clearance over the pivots at zero load) is defined as:

$$C_B = R_B - R_S = R_P - a - R_S.$$

From the definition of C_P and the equation above, it is seen that

$$a = C_P - C_B.$$

The preload coefficient is defined as:

$$m = 1 - \frac{C_B}{C_P} = 1 - \frac{(R_P - a - R_S)}{R_P - R_S} = \frac{a}{R_P - R_S}.$$

Under load, the shaft center will move away from the bearing center. Also, each pad will incline such that the resultant of the fluid film pressures passes through the pivot point. Its center of curvature will, therefore, move along an arc of a circle, whose center is the pivot point.

Let e_B = distance between the shaft center and the bearing center under a given

load on the shaft (bearing concentricity).

Let e_p = distance between the shaft center and the center of curvature of a pad, under same load on the shaft (pad eccentricity).

We then define two eccentricity ratios as follows:

Pad eccentricity ratio is:

$$\epsilon_p = \frac{e_p}{C_p}$$

and bearing eccentricity ratio is:

$$\epsilon_B = \frac{e_B}{C_B}$$

Test Bearing Design

The numerous variables in the design of a tilting-pad journal bearing can be grouped into those describing the design of the individual pad; those which determine how the pads are assembled together into the bearing and those which describe the pivot. The pad design variables and the values chosen for the test bearing include:

- (a) Clearance ratio (C/R) - 3×10^{-3} in/in.
- (b) Slenderness ratio (L/D) - 1.0
- (c) Arc length (β) - 80 degrees
- (d) Position of the pivot along the pad arc (which will determine the direction of the resultant of the fluid film forces acting on the pad since this must pass through the pivot) - 44 degrees from leading edge, or .55 of the arc length.

The variables describing the assembly of pads into the bearing are:

- (a) The number of pads - 4
- (b) The preload, m - adjustable to any value, $0 < m < 1$.

The pivot design variables depend on the exact pivot configuration chosen, but for the sphere in contact with an internal cylindrical surface, as is used here, they are:

- (a) Material modulus of elasticity - 30×10^6 psi for hardened tool steel
- (b) Radius of the sphere - .625 inch
- (c) Radius of the cylinder - .655 inch

The position of the pivots was chosen as representing the best probable compromise between the improved load capacity to be obtained from a position behind the midpoint and yet avoiding the confusion and uncertainty caused by multiple values of calculated load capacity for the normal range of operating eccentricities. It is expected that experiments will be performed for two values of preload coefficient, probably 0.5 and 0. The principal guidelines in planning the pivot design were to hold the Hertzian contact stress below 200,000 psi while minimizing relative sliding of the contacting surfaces. The elastic stiffness of the pivot contacts has been calculated. The stiffness varies as the $2/3$ power of the pad load and is 1.3×10^6 lb/in. at 500 lb. load. This is within an order of magnitude of the expected fluid-film stiffness; therefore, pivot deflection will be a factor to be considered both with respect to the overall bearing stiffness and because of the tendency to reduce bearing preload at high values of static load. The test bearing pivots are about as stiff as they can reasonably be if the self-aligning feature of the bearing is to be retained (a cylinder contacting a cylinder would be stiffer but would pivot in one plane only). Therefore, this is a property of the bearing which is encountered in turbomachinery as well as in the test bearing and it will be factored into the calculations that are made for comparison of theoretical and test data. It is planned to compare the experimental and theoretical results in this program by using the calculated bearing characteristics in a rotor-bearing analysis of the test machine and comparing calculated and measured response orbits and critical speeds. Pivot stiffnesses will be included in the pedestal characteristics in the calculations just as we would expect to do in a design analysis.

THEORETICAL ANALYSIS OF THE TILTING-PAD BEARING IN THE TURBULENT FLOW REGIME

Broadly speaking, the theoretical analysis for the tilting-pad bearing is constructed by summation of the effects of the individual pads which are determined from the lubrication theory for fixed, partial-arc journal bearings. There are additional factors and complications to be considered as will be shown, but this is the essence of the procedure which is followed. The stepwise development of the tilting-pad bearing theory beginning with the linearized turbulent flow theory for the individual fixed partial arc, then to the individual tilting pad, and finally to the composite bearing will be described briefly in the following sections. The analysis and the numerical solution of the resulting equations are described in more detail in the Appendices.

Linearized Turbulent Lubrication Theory for a Partial-Arc Bearing

The development of the linearized, turbulent-flow lubrication theory based on the eddy diffusivity concept was described by Ng and Pan in Reference 5. The mathematical analysis leading to the theory was given also in an Appendix to Reference 6 and the procedure for numerical integration of the turbulent lubrication equation for calculating static and dynamic load characteristics of a single-bearing element was presented in the final report (Ref. 1). This theory overcomes the two main objections to the earlier turbulent lubrication theory of Constantinescu (Ref. 7), namely:

- 1) ~~Discontinuity in the shear stress at the edges of the laminar sublayers,~~
- 2) Improper treatment of non-planar flow in the finite length bearing analysis.

All of the turbulent-flow lubrication theories are based on concepts of turbulent flow which were originated in connection with pipe or channel flows. There is no provision for considering the unstable, vortex flow which generally occurs in bearings before fully-developed turbulence and there is no theoretical basis for applying the turbulent lubrication theory to bearings operating in this region. This void in the lubrication theory is one reason why fundamental studies of flow between eccentric cylinders are being performed in this program. It is fortuitous that the turbulent-flow lubrication theory does perform well enough in the vortex flow region to be useful for design calculations. This is because the sudden

change in bearing performance coincides with the expected transition to vortex flow and the measured performance curves remain smooth and regular through the region where transition to fully-developed turbulence should occur (Ref. 4). The same sort of behavior was found in the friction torque measurements between eccentric cylinders which were reported earlier (Ref. 2).

The solution of the linearized, turbulent-flow lubrication theory has been extended to calculate the frictional loss and lubricant flow as well as the static and dynamic load characteristics of the individual pad. The numerical solution is discussed in detail in Appendix A.

Dynamic Load Analysis of the Partial-Arc Bearing

The dynamic load analysis of the individual partial-arc bearing is based on an examination of small motions of the journal center about its equilibrium position. The analysis is limited to small motions because the resultant of the hydrodynamic fluid-film forces is a non-linear function of the displacement, attitude angle, and velocity of the journal center. Therefore, the agreement between the analysis and the behavior of practical rotor systems depends, in part, on how closely the relationship between the gradient of the bearing film force and the shaft center displacement approaches linearity in the region of interest. In most hydrodynamic journal bearings, this relationship is reasonably linear for values of eccentricity ratio up to about 0.8. Above this eccentricity ratio, the curvature of the force-displacement curve increases sharply. Ordinarily, design loads for high-speed rotating machinery result in equilibrium eccentricity ratios well within the useful range of the dynamic analysis.

In the dynamic analysis, the fluid-film force resultant is reduced to a set of spring and damping force coefficients. The values of these force coefficients are the gradients of the force-displacement and force-velocity curves at the equilibrium position of the journal center. In principle, this system is analogous to a mechanical system of springs and dashpots supporting the shaft. However, there are significant differences:

- (1) The bearing film force vs. displacement and force vs. velocity relationships are non-linear so the spring and damping coefficients are not constant but vary continuously with the equilibrium position of the shaft

center. In the case of turbulent flow bearings, the coefficients change also with Reynolds number.

- (2) There is a cross-coupling effect, arising from the fact that the resultant of the film forces caused by a displacement or velocity of the shaft center, is not co-linear with the displacement or velocity. Thus, if the shaft is displaced, or if a velocity is imparted to it, the resulting change in fluid-film force will have components both along the direction of displacement, or velocity, and normal to it.

If the dynamic fluid-film force and the shaft displacement and velocity are resolved into components along x and y coordinates with the steady-state load (F_o) directed along the x axis, we have:

$$F_x - F_o = -K_{xx}x - B_{xx}\dot{x} - K_{xy}y - B_{xy}\dot{y}$$

$$F_y = -F_{yx}x - B_{yx}\dot{x} - K_{yy}y - B_{yy}\dot{y}$$

where the first subscript defines the direction of force and the second subscript defines the direction of the displacement or velocity. The eight coefficients have been calculated for the fixed, 80 degree, arc bearing in the manner described in Appendix B for Reynolds' numbers up to 12,000 and for equilibrium eccentricity ratios from 0.01 to 0.99.

Dynamic Analysis of the Tilting Pad

The small motions of the shaft center caused by dynamic load will cause the individual tilting pad to oscillate about its pivot point. Under certain conditions of bearing operation and pad design, this oscillation will approach a resonance. When this happens, the stiffness of the pad fluid film will fall off sharply. For typical pad designs, resonance will occur when the pad eccentricity ratio is small and, therefore, the load on that particular pad will be light. In addition, the effects of fluid-film damping, which will be large for small eccentricity, and of the mass inertia of the pad about its pivot will provide some support at the pad resonance condition. It may be that the most serious effects of pad resonance are on the pivots where fretting may be brought on by large oscillation amplitudes at

high frequency. A comparatively large bearing preload should help to avoid pad resonance by avoiding low eccentricity ratios for the pads on the side of the bearing away from the static load direction.

The analysis to determine the critical mass of the pad for resonance with the effects of pad inertia ignored is given in Appendix B. This analysis can be used to calculate the dimensionless pad critical mass as a function of bearing Sommerfeld number for different values of Reynolds number, once the pad fluid film dynamic characteristics are determined from the turbulent lubrication analysis for the fixed pad. This has been done and the results will be presented later in this report. They can be used in bearing design to assure proper tracking and to avoid having a pad resonance at or near the normal machine operating conditions.

Analysis of the Composite Tilting-Pad Bearing

The static and dynamic load characteristics of the composite, tilting-pad bearing are determined by summation of the effects of the individual pads. The procedure for doing this is long and tedious. Briefly, it is required that the total force component in the y-direction (normal to the load line) summed over all pads must be zero. For a given eccentricity ratio and bearing preload, several values of attitude angle are assumed. The individual pad forces resulting from each of these assumed journal positions are determined from the data for a single, fixed bearing pad. The summation of the pad forces for each assumed attitude angle are plotted and, by interpolation, the attitude angle where the summation of forces in the y-direction is zero is determined. The individual pad forces can then be analyzed again for the correct attitude angle. The procedure can be simplified a great deal if the pad pivots are located symmetrically about the x-axis or static load line and if pad inertia is neglected. In this event, the attitude angle will always be zero and, moreover, since the force and displacement vectors are now co-linear, the cross-coupling spring and damping coefficients vanish. Furthermore, for the four-pad bearing with the load line between the pivots, there is also symmetry about the y-axis so the dynamic coefficients in the x- and y-directions will be identical and the response of the shaft to a rotating load will always be a circle.

The analysis for dynamic characteristics of the composite tilting-pad bearing is given in more detail in Appendix B.

Calculated Static and Dynamic Characteristics for the Tilting-Pad Bearing

As a check, some static load results were calculated for laminar flow for comparison with Raimondi and Boyd's results (Ref. 9) for partial-arc bearings with laminar flow. The calculated values (in parentheses) are compared with Raimondi and Boyd's results in the table below.

L/D = 1.0 60° Arc (mesh: circumferential-16, axial -14)						
ϵ	ϕ	$\frac{R_f}{C}$	$\frac{Q}{RCNL}$	Q_s/Q	S	
0.1	67.92 (65.35)	29.1 (28.86)	3.07 (3.05)	.0267 (0.0212)	8.52 (8.59)	
0.8	18.33 (18.26)	1.42 (1.39)	.883 (0.836)	.200 (0.159)	0.101 (0.102)	

L/D = 1.0 120° Arc (mesh: circumferential-16, axial -14)						
ϵ	ϕ	$\frac{R_f}{C}$	$\frac{Q}{RCNL}$	Q_s/Q	S	
0.1	72.43 (71.99)	14.5 (14.20)	3.20 (3.19)	.0876 (0.0777)	2.14 (2.135)	
0.8	27.42 (27.28)	1.27(1.195)	1.57 (1.428)	0.535 (0.484)	.0531 (0.0529)	

L/D = 1.0 Full Journal (mesh: circumferential-20, axial -14)						
ϵ	ϕ	$\frac{R_f}{C}$	$\frac{Q}{RCNL}$	Q_s/Q	S	
0.1	79.5 (83.73)	26.4 (24.8)	3.37 (3.39)	0.150 (0.144)	1.33 (1.30)	
0.8	36.24(36.13)	1.7 (1.38)	4.62 (4.78)	0.842 (0.820)	.0446 (.043)	

The agreement seems quite satisfactory.

Calculations of static load capacity, dynamic coefficients, friction torque and flow through the bearing have been made for a four-pad bearing with the static load line directed midway between pivots. Consistent with the test bearing design, the pad arc-length is 80 degrees and the pivot is located at .55 of the arc length (44 degrees) from the leading edge.

Static load capacity results are given in Figures 4 through 7 respectively for preload coefficients of 0, 0.3, 0.5 and 0.7 respectively. The results are presented as Sommerfeld number plotted against eccentricity ratio for various values of Reynolds numbers.

up to 16,000. In constructing the design curves for smaller preloads ($m = 0$ and 0.3), the problem of two branches of the curve of pad force plotted against $\epsilon \cos \phi$ must be faced. In effect, this means that for a given pad force or load there are two values of eccentricity, and two angles of pad inclination which might occur. The difference in load-carrying capacity is not great, and in this case, the position of lesser pad inclination was chosen for the bearing design curves.

The locus of attitude angle vs. eccentricity ratio for the individual pad with 0.55 pivot position is given in Figs. 8 and 9 for Reynolds numbers up to 16,000. It is clear that ϵ and ϕ are single-valued. The attitude angle vs. eccentricity ratio locus for the composite bearing is simply the x-axis, $\phi_o = 0$ for all ϵ , because of symmetrical positioning of the pivots about that line.

The dynamic bearing characteristics are plotted as dimensionless stiffness ($\frac{C}{W} K$) or damping ($\frac{C}{W} \omega B$) vs. Sommerfeld number for the various values of Reynolds numbers in Figs. 10 through 17 for $m = 0, 0.3, 0.5$, and 0.7 respectively. There is only one spring and one damping coefficient to describe the bearing dynamic characteristics completely because of symmetry of the pivots with respect to both x- and y-axis and because of the assumption of inertialess pads.

A programming error has been found in the friction torque calculations. This has been corrected, but the revised results are not yet available. They will be given in the next progress report.

Dimensionless flow vs. Sommerfeld number is plotted in Figs. 18 through 21 for the different preloads.

Finally, the dimensionless critical mass of the pad is given as a function of Sommerfeld number in Figs. 22 through 25. There are separate values of critical mass for the pads which are on the side away from the load and for those on the loaded side. Except for the cases of lower preload ($m \leq 0.3$), the smaller of the two values are plotted. For the low preload cases the top pads will nearly always be completely unloaded so the critical mass for the bottom pad is plotted.

DYNAMIC LOAD JOURNAL BEARING APPARATUS

Mechanical Components

The same apparatus which was used in the previous program and described in detail in References 1 and 6 will be used in this program with some modifications. The basic arrangement of the mechanical elements of the apparatus is shown schematically in Fig. 26. A preloaded pair of angular contact ball bearings provide support at one end of the long shaft with the test bearing supporting the other end. The shaft diameter is four inches and the span between bearings is 40 inches. The shaft is driven by a 7.5 H.P., variable speed (1770 to 11,500 rpm) electric drive coupled to the support bearing end by a specially-balanced, flexible disk coupling. Unidirectional, downward load is applied to the inboard ball bearing at the test bearing end of the shaft through a cable by a large, low spring rate (125 lb/in.) compression spring. A rotating load is applied in one of two ways. For independent control of load frequency and direction, unbalance weights are attached to the outer race housing of a ball bearing whose inner race is mounted on the shaft. The housing and outer race are driven in either direction by a small universal electric motor through a flexible-disk coupling. Synchronous unbalance load is applied by replacing the rotating load bearing with a disk to which unbalance weights can be attached.

The apparatus is capable of investigating bearing performance over the following range of conditions:

- Reynolds Number - up to 12,000 (for $C/R = 3 \times 10^{-3}$ in/in.)
- Static Load - up to 1000 lb.
- Rotating Load - up to 100 lb.
- Rotating Load Frequency - 2000 to 20,000 cpm in either direction.

The lubricant which is normally used is a silicone oil of 0.65 cs viscosity at 77 F and a viscosity-temperature coefficient $(1 - \frac{\text{viscosity at 210 F}}{\text{viscosity at 100 F}})$ of 0.31. It can be delivered under pressure and at controlled temperature to any of a number of points on the bearing housing depending on the bearing being tested. There are close clearance seals outboard of the test bearing and beyond them are cavities from which the lubricant is scavenged.

Instrumentation

For the tilting-pad test bearing, the following measurements will be made:

- a) Locus of the shaft center within the bearing clearance
- b) Dynamic component of force applied by the shaft to the bearing
- c) Dynamic motion of the shaft at test bearing and support bearing ends
- d) Oscillating motion of one of the pads about its pivot in both pitch and roll
- e) Steady-state and rotating load magnitude
- f) Friction torque of the test bearing
- g) Lubricant film temperature

The shaft locus and shaft and pad motion measurements are made by eddy current displacement sensors. The performance of these sensors is not affected by whether there is air or silicone fluid in the gap between the probe tip and the reference surface since both are good dielectrics. However, they are affected by temperature. The shaft displacement measuring probes are mounted on rings located outboard from the seal and scavenging rings on both ends of the test bearing where the temperature remains nearly uniform. The outputs of the two vertical probes are averaged by adding them together using a summing amplifier, and the same is done for the two horizontal probes. This arrangement minimizes the effects of any bending of the shaft under dynamic load at high eccentricity. Four probes are mounted in the ring in which the bearing pivots are mounted to measure pitch and roll (circumferential and axial oscillation) of one of the pads. Two probes in a push-pull arrangement feeding into a summing amplifier measure each motion. Temperature effects are minimized in this way. The instrumented pad can be put in any position relative to the static load by rotating the bearing pivot ring in the test bearing housing. Two probes are mounted on the support bearing housing to measure vertical and horizontal displacement of the shaft at that end. The displacement probes have been calibrated in a bench micrometer fixture with direct reading divisions of one micron using the same material as the shaft is made of for the reference surface. The sensitivity of all probes was adjusted to give matched outputs of 0.002 inches \pm 0.00005 inches per volt.

Piezoelectric crystal force gages are used to hold the pivot ring of the test bearing in place in the housing in order to measure the dynamic force transmitted

to the bearing from the shaft. The high stiffness, 5×10^6 lb/in. and great sensitivity to dynamic load changes, 10 mv/lb. output, together with high static-load capacity, 5000 lbs., of these gages fit them extremely well for this application. The force gages are calibrated by applying known loads in known directions to the shaft through the steady-state load bearing with the shaft rotating and recording the reaction on the oscilloscope.

The shaft locus within the test bearing is displayed on one oscilloscope by feeding the horizontal and vertical outputs into the x and y scope axis. In addition, any pair of dynamic components of shaft motion, force, or pad motion can be switched into the inputs of a second dual trace oscilloscope where they can be displayed on the x-y axis or as two signals on a common time base. Variable electronic filters set for band pass operation are placed ahead of the inputs to this oscilloscope to eliminate unwanted high-frequency noise or subharmonic signals caused by fractional frequency whirl. A strain gage load cell has been added to the attachment mount for the cable which applies the static load to the shaft. This arrangement supplants measurement of load spring deflection as a means for measuring and controlling the static load magnitude. Rotating load magnitude is determined by using unbalance slugs of known weight at a known radius with a known rotational speed.

Test bearing frictional torque will be measured by a Lebow-strain gage type, rotary torque sensor coupled into the drive between the motor and the support bearing end of the shaft. Based on approximate calculations of test bearing torque, a 200 in-lb. (with 50 percent permissible overload) unit rated for speeds up to 13,000 rpm was selected.

PRELIMINARY EXPERIMENTS

The only feasible means for obtaining precise test bearing torque measurements in the dynamic load test rig require that the torquemeter be inserted in the drive train between the drive motor and the support-bearing end of the shaft. This means that the torquemeter will measure parasitic torques from the support and loader bearings also. Estimated torques for the test bearings and the support and loader bearings were calculated and are given in Fig. 27. The test bearing torque was estimated from the charts of bearing friction given in Reference 2 which are based on the data of Wendt, Vohr, and Smith and Fuller.

Torque for the bearing, assuming laminar flow, was obtained by using the results of Raimondi and Boyd (Ref. 9). The torques for the ball bearings used as load and support bearings were estimated using the friction coefficients suggested by Palmgren. It is apparent that the parasitic torques should be small as compared to the test bearing torque. Still, especially for low speeds and high loads, the parasitic torques may be nearly 10 percent of the test bearing torque. Also, from previous experience with the relationships used to estimate test bearing torque, it is expected that estimated torques will be on the high side, perhaps as much as 50 percent high. Therefore, it was decided to perform some preliminary experiments in which the parasitic torques would be determined.

An externally pressurized, gas-lubricated bearing was designed and fabricated to take the place of the test bearing. Calculated static load capacity of this bearing is approximately 400 pounds for a pressure ratio of 10. The computed threshold speed for whirl for the same pressure ratio is 38,000 rpm. This bearing has been installed in the apparatus and experiments to determine the parasitic torque have begun.

Thus far it has been possible to get data only for very low loads because the facilities which will supply large volume flow of high pressure gas to the gas bearing are not yet complete. Data have been obtained for a 50 pound load, and these are given in Fig. 28. The gas bearing torque calculated using the Petroff equation has been subtracted from the total torque to obtain the parasitic torque. The results are in good agreement with expectations.

The performance of the apparatus, including instrumentation and especially the torquemeter, was entirely satisfactory during this experiment. Operation was limited to 8000 rpm because of concern over hydrodynamic instability of the gas-lubricated bearing at the low pressure ratio, about 3.0, which could be obtained during this experiment.

FLOW STABILITY EXPERIMENTS

Use of Electrochemiluminescent Flow Visualization Technique for the Study of Flow Patterns in a Glass Journal Bearing with Close Clearances

Chemiluminescence is the generation of light by purely chemical means. Electrochemiluminescence is the generation of light by chemical means wherein the usual chemical catalyst is replaced by an electrical stimulation. This latter process has been shown by Howland, Pitts and Gesteland (Ref. 10) to be a very effective means of displaying boundary layer flow along surfaces immersed in a chemiluminescent solution. Apparently, the process works in the following way. A potential difference is maintained between the surface to be studied and a reference electrode located elsewhere in the solution. Flow of electric current stimulates the emission of a chemiluminescent glow right at the anodic surface. The intensity of this glow depends on the rate of mass transfer of fresh reactants into the boundary layer along the anodic surface. Thus, if the boundary layer is turbulent, the turbulent eddies show up as variations in the intensity of the chemiluminescence. Test photographs made by Howland, Pitts and Gesteland (Ref. 10) show that this flow visualization technique revealed boundary layer flow patterns with excellent clarity.

The electrochemiluminescent flow visualization technique has two characteristics which make it appear promising for studying flow patterns in bearings. The first is that this technique does not interfere in any way with the flow. This is of obvious importance in bearings where the clearances are very small and where visual techniques involving suspended particles would be impossible to use. The second advantageous characteristic of the electrochemiluminescent technique is that the glow is apparently confined to an extremely thin layer next to the anode surface. Howland and co-workers have conjectured that at certain alkalinity levels of the solution, the glow may take place entirely within a few wavelengths of the surface. This also makes this visualization technique ideally suited for the close clearances of bearing flows.

The experimental setup with which we propose to study bearing flows by electrochemiluminescence is shown schematically in Fig. 29. The transparent glass bearing simply will be a length of precision bore Pyrex glass tubing of one inch I.D. Such

tubing is inexpensive and has very accurately controlled tolerances. The inside surface of this glass bearing will be coated with a thin, transparent, vacuum deposited layer of platinum and will be the anodic surface for the electrochemiluminescent process, i.e., the surface at which light is generated. The journal will be an accurately ground steel shaft, also platinum plated, and will serve as the cathode. The outer glass bearing will be supported by the pivoted loading arm shown in Fig. 29. The journal will be driven at speeds up to 10,000 rpm by an air turbine or a coupled electric drive. The whole test bearing will be immersed in the chemiluminescent solution as shown.

The radial clearance between the cylinder and the journal for the initial experiment will be .005 inches, which results in a clearance-to-radius ratio of $C/R = .01$. In later experiments this may be reduced still further.

Although the electrochemiluminescent visualization technique appears promising with regard to studying bearing flows, there are still a number of factors which may negate or limit its feasibility for lubrication studies. The most critical unknown factor concerns the time scale of the turbulence. Since the journal will be rotating very rapidly at conditions of turbulence, the frequency of the turbulent fluctuations and hence the rate of change of random turbulent flow patterns may be too rapid to be photographed. Preliminary testing of the electrochemiluminescent technique will be carried out to try to answer this and other questions before constructing the test rig shown in Fig. 29. In any case, this test rig will not be expensive, and it is believed that the potential usefulness of the electrochemiluminescent technique is such as to make it worthwhile to spend some time investigating it.

Torque Measurements to Determine Flow Instabilities Between Eccentric Cylinders with Close Clearance

As mentioned earlier in this section, the experiments on flow stability performed at MTI last year included detection of the onset of Taylor vortices by torque measurements and also measurement of friction factors at different eccentricities. The measured critical speeds for onset of Taylor vortices were not in good quantitative agreement with the simplified theoretical predictions of DiPrima (Ref. 3), the theoretical values of critical speed being substantially lower than measured

values. This discrepancy may be due to inertia effects in the flow that are not considered in the theoretical analysis. At the Taylor critical speed, the ratio of inertia terms to viscous terms in the equations of motion for the flow are proportional to C/R . To see if inertia effects were significant in the flow stability experiments performed last year at MTI, it is planned to repeat these experiments at a substantially reduced C/R ratio, namely $C/R = .01$. This will be accomplished with the presently existing flow-stability test rig using a new, close clearance, aluminum, outer cylinder.

In addition to measuring Taylor vortex critical speed with the close-clearance cylinder, friction factor measurements will also be made at different eccentricities. For concentric cylinders (inner cylinder rotating) the friction factor is approximately proportional to $(C/R)^{0.2}$. For eccentric cylinders it is not known how the friction factor depends on C/R . The proposed close-clearance friction factor measurements combined with the previous MTI friction factor measurements should indicate what this dependence is.

It should be pointed out that once the dependence of Taylor critical speed and eccentric friction factor on C/R is approximately established, the results of the MTI flow stability experiments can be extrapolated to actual bearing clearance ratios.

Visual Study of Flow Stability in Partial-Arc Bearing Configuration

Flow stability will be studied visually for a partial-arc bearing configuration with a relatively large radial clearance, i.e., $C = 1/16$ inch. These experiments will be conducted using the present flow stability test rig with a new partial-arc outer cylinder, the design for which is shown in Fig. 30. This new outer cylinder will consist basically of a solid aluminum cylinder with an 80 degree partial-arc Plexiglas bearing mounted concentrically within it. The aluminum cylinder will be cut away outside of the Plexiglas partial-arc to permit viewing of the flow pattern through the Plexiglas. Flow visualization will be by means of a suspension of fine aluminum powder in silicone oil. Five pressure taps will be used to measure the pressure distribution circumferentially along the bearing. The axial length of the partial-arc bearing will be approximately two feet. The onset of Taylor vortices and turbulence at various converging and diverging geometries of this partial-arc bearing will be studied and the results compared with theory.

FUTURE WORK

Preliminary studies preparatory to development of a theoretical analysis of the floating-ring bearing in the turbulent flow regime have just begun. Some difficulties have become apparent but this analysis should be completed in the next quarter.

Determination of the parasitic torque characteristics of the dynamic load bearing apparatus should be completed in the next month. The tilting-pad test bearing should then be available and the measurements of bearing static and dynamic load characteristics can begin. Design of the floating-ring test bearing will be completed and fabrication will begin during the next quarter.

Materials have been ordered for preliminary experiments to evaluate the feasibility of the electrochemiluminescent technique for flow visualization between close clearance cylinders. Construction of the test rig shown in Fig. 30 will await the results of these preliminary tests. The measurements of torque between close-clearance cylinders and the study of flow between a rotating inner cylinder and a partial-arc outer surface will be performed after the electrochemiluminescent studies.

REFERENCES

1. Orcutt, F. K. and Arwas, E. B., "Analysis of Turbulent Lubrication, Volume 1, The Static and Dynamic Properties of Journal Bearings in Laminar and Turbulent Regimes", MTI 64TR19, Final Report to NASA on Contract NAS-W-771, May 1964.
2. Vohr, J. H., "Analysis of Turbulent Lubrication, Volume 2, An Experimental Study of Vortex Flow and Turbulence in Concentric and Eccentric Annuli", MTI 64TR20, Final Report to NASA on Contract NAS-W-771, May 1964.
3. DiPrima, R. C., "A Note on the Stability of Flow in Loaded Journal Bearings", Trans. ASLE, Vol. 6, No. 3, July 1963, pp 249-253.
4. Orcutt, F. K., "Investigation of a Partial Arc Pad Bearing in the Superlaminar Flow Regime", ASME Paper 64-LubS-8, presented at the Lubrication Symposium at Cleveland, Ohio, April 1964.
5. Ng, C. W. and Pan, C. H. T., "A Linearized Turbulent Lubrication Theory", ASME Paper to be presented at the International Lubrication Conference, Washington, D.C. October 1964.
6. Arwas, E. B., Orcutt, F. K., and Vohr, J. H., "Lubrication Analysis in Turbulent Regime", 2nd Quarterly Report, Contract NAS-W-771, January 1964.
7. Constantinescu, V. N., "Analysis of Bearings Operating in Turbulent Regime", J. of Basic Engr., Trans. ASME, Series D, Vol. 84, 1962, pp. 139-151.
8. Smith, M. I., and Fuller, D. D., "Journal Bearing Operation at Superlaminar Speeds", Trans. ASME, Vol. 78, 1956, p. 469.
9. Raimondi, A. A. and Boyd, J., "A Solution for the Finite Journal Bearing and its Application to Analysis and Design: III," Trans. ASLE, Vol. 1, No. 1, 1958.
10. Howland, B., Pitts, W. and Gesteland, R., "Use of Electrochemiluminescence for Visualizing Fields of Flow", Technical Report 404, Mass. Inst. of Tech., Research Laboratory of Electronics, 1962.
11. Pinkus, O. and Sternlicht, B., "Theory of Hydrodynamic Lubrication", McGraw-Hill, 1961.
12. Ng, C. W., Elrod, H. G., "Nonlinear Turbulent Lubrication Theory", MTI Report 1964 (to be issued).
13. Lund, J. W., "Spring and Damping Coefficients for the Tilting Pad Journal Bearing", ASLE Preprint 64AM233.

APPENDICES

APPENDIX A

NUMERICAL ANALYSIS FOR LINEARIZED, TURBULENT, INCOMPRESSIBLE, FULL AND PARTIAL JOURNAL BEARINGS

This section describes the Reynolds equation for linearized turbulent lubrication theory and its finite difference form. Boundary conditions are given for the full journal and partial arc bearing. Expressions of flow and torque are given. Finally, the iteration convergence and extrapolation are discussed in detail.

Reynolds Equation for Turbulent Lubrication

Let the flow per inch in the fluid film be denoted Q with the component Q_x and Q_z . Then, from the thin film approximation of Stokes Eq. (see Ref.11).

$$(1) \quad Q_x = \frac{1}{2} R\omega\bar{h} - G_x \frac{\bar{h}^3}{\mu} \frac{\partial \bar{P}}{\partial x}$$

$$(2) \quad Q_z = -G_z \frac{\bar{h}^3}{\mu} \frac{\partial \bar{P}}{\partial z}$$

where

\bar{P} = pressure, psi

\bar{h} = film thickness, inch

μ = viscosity of lubricant, lb.sec/in²

R = journal radius, inch

ω = angular velocity, rad/sec.

G_x, G_z = flow parameter, equal to $\frac{1}{12}$ for laminar flow and for turbulent flow, they are functions of Reynolds Number (linearized theory) and pressure gradient in the flow direction as well perpendicular to it, (non-linear theory) see References 5 and 12.

The continuity equation gives: -

$$(3) \quad \frac{\partial}{\partial x} (Q_x) + \frac{\partial}{\partial z} (Q_z) + \frac{\partial \bar{h}}{\partial t} = 0$$

Introduce Eqs. (1) and (2)

$$(4) \quad \frac{\partial}{\partial x} \left[G_x \frac{\bar{h}^3}{\mu} \frac{\partial \bar{P}}{\partial x} \right] + \frac{\partial}{\partial z} \left[G_z \frac{\bar{h}^3}{\mu} \frac{\partial \bar{P}}{\partial z} \right] = \frac{1}{2} R \omega \frac{\partial \bar{h}}{\partial x} + \frac{\partial \bar{h}}{\partial t}$$

To make dimensionless, set

$$\begin{aligned} h &= \bar{h}/C = 1 + \epsilon \cos(\theta - \phi) \\ P &= \bar{P}/\mu N \left(\frac{R}{C}\right)^2, \quad \omega = 2\pi N \\ x &= \bar{x}/D, \quad z = \bar{z}/L, \quad \theta = \bar{x}/R = 2x \end{aligned}$$

Hence the dimensionless Reynolds Equation has the form.

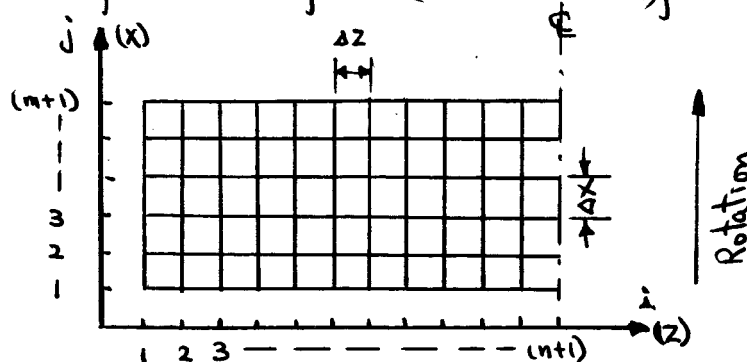
$$(5) \quad \frac{\partial}{\partial x} \left[G_x h^3 \frac{\partial P}{\partial x} \right] + \left(\frac{D}{L}\right)^2 \frac{\partial}{\partial z} \left[G_z h^3 \frac{\partial P}{\partial z} \right] = 8\pi \left[\frac{\dot{\epsilon}}{\omega} \cos(\theta - \phi) + \left(\frac{\epsilon\dot{\phi}}{\omega} - \frac{\epsilon}{2}\right) \sin(\theta - \phi) \right]$$

Finite Difference Equations: -

The Reynolds Equation is solved numerically by finite difference methods.

The bearing film is subdivided into a mesh shown in the figure below. Eq. (5) can be written in the finite difference form.

$$(6) \quad P_{ij} = \frac{\left\{ \begin{aligned} &-8\pi(\Delta x)^2 \left[\frac{\dot{\epsilon}}{\omega} \cos(\theta - \phi) + \left(\frac{\epsilon\dot{\phi}}{\omega} - \frac{\epsilon}{2}\right) \sin(\theta - \phi) \right]_{ij} \\ &+ G_x h^3|_{i,j+\frac{1}{2}} P_{i,j+1} + G_x h^3|_{i,j-\frac{1}{2}} P_{i,j-1} \\ &+ \left(\frac{D}{L}\right)^2 \left(\frac{\Delta x}{\Delta z}\right)^2 \left[G_z h^3|_{i+\frac{1}{2},j} P_{i+1,j} + G_z h^3|_{i-\frac{1}{2},j} P_{i-1,j} \right] \end{aligned} \right\}}{G_x h^3|_{i,j+\frac{1}{2}} + G_x h^3|_{i,j-\frac{1}{2}} + \left(\frac{D}{L}\right)^2 \left(\frac{\Delta x}{\Delta z}\right)^2 \left[G_z h^3|_{i+\frac{1}{2},j} + G_z h^3|_{i-\frac{1}{2},j} \right]}$$



The boundary conditions are: -

$$i = 1 \quad P_{1,j} = 0$$

$$i = n+1 \quad P_{n+2,j} = P_{n,j}$$

$$j=1 \quad P_{i,1} = \begin{cases} P_{inlet} & \text{partial arc} \\ P_{i,m+1} & \text{full journal} \end{cases}$$

$$j = n+1 \quad P_{i,m+1} = \begin{cases} P_{outlet} & \text{partial arc} \\ P_{i,1} & \text{full journal} \end{cases}$$

$$i,j \quad \text{If } (P_{i,j})_{\text{calculated}} < P_{\text{cavitation}} \Rightarrow P_{ij} = P_{\text{cavitation}}$$

The pressure is initially set equal to zero and Eq. (6) is then solved by iteration. Pressure derivatives are found from the pressure distribution and they will be used to compute the dimensionless frictional force and flow.

The load carrying capacity is calculated from

$$(7) \quad f_r = -2 \int_0^{\frac{1}{2}} \int_{\theta_{in}}^{\theta_{out}} P \cos(\theta - \phi) dx dz = -2\Delta x \cdot \Delta z \sum_{i,j} P_{i,j} \cos(\theta_{i,j} - \phi)$$

$$(8) \quad f_t = 2 \int_0^{\frac{1}{2}} \int_{\theta_{in}}^{\theta_{out}} P \sin(\theta - \phi) dx dz = 2\Delta x \cdot \Delta z \sum_{i,j} P_{i,j} \sin(\theta_{i,j} - \phi)$$

$$\frac{W}{\mu NDL \left(\frac{R}{C}\right)^2} = \frac{1}{S} = \sqrt{f_r^2 + f_t^2}$$

$$\phi_{calc} = \tan^{-1} (f_t / f_r)$$

where f_r is the dimensionless radial force component, f_t is the tangential component, S is the Sommerfeld number and ϕ_{calc} is the calculated attitude angle.

The indicated summations are computed by Simpson rule of integration, i. e.,

$\frac{1}{3} \Delta [P_1 + 4P_2 + 2P_3 + 4P_4 + \text{-----}]$ and if either m or n are odd the first interval is integrated by $\frac{1}{12\Delta} [5P_1 + 8P_2 - P_3]$. In addition end corrections are made at the boundary to the ruptured film.

The dimensionless flow components are expressed by

$$\frac{Q_x}{RCNL} = h\pi - h^3 G_x \int_0^1 \frac{\partial P}{\partial \theta} dz'$$

$$\frac{Q_z}{RCNL} = -\frac{1}{2} \left(\frac{D}{L}\right)^2 \int_0^{2\pi} h^3 G_z \frac{\partial P}{\partial z} d\theta$$

And the dimensionless frictional force is defined as,

$$\bar{F} = \frac{h^2 FC^2}{\mu \nu RL} = \int_{-\frac{1}{2}}^{\frac{1}{2}} \int_0^{2\pi} \frac{\tau_w^*}{h^2} d\theta dz$$

where

$$\tau_w^* = \tau_c^* + \frac{1}{2} \text{grad } P$$

$$\tau_c^* = \rho V^2 C_f / 8$$

$$\text{grad } P = \text{Re}_{\text{local}} \cdot \left(\frac{h^3}{2\pi} \frac{\partial P}{\partial \theta} \right)$$

$$C_f = 8\tau^*/\text{Re}^2 \quad \text{and} \quad \tau^* = \tau h^2 / \mu \nu$$

During the computation of the wall shear stress it is to be noted that the cavitation is taken into consideration, e.g. when the pressure is zero or negative, the area would be reduced by the ratio of $h_{\min}/h_{\text{local}}$ to take care of the area reduction due to cavitation. It is also known as the shear effect in cavitation which can be verified easily from continuity considerations. Also the frictional coefficient is given in the form of $2\tau/\rho V^2$ which is conventionally used to study the flow between rotating cylinders. The definitions of G_x , G_z , and C_f , are given in Reference 5.

Iteration Convergence and Extrapolation

The convergence of the pressure iteration is tested by two methods, which shall be denoted relative convergence and absolute convergence. The relative convergence is tested as follows: after the k'th pressure iteration compute:

$$(9) \quad \frac{\sum_i \sum_j |P_{i,j}^{(k)} - P_{i,j}^{(k-1)}|}{\sum_i \sum_j P_{i,j}^{(k)}} \delta_R = \Delta_R$$

where δ_R is given by the input. When Δ_R becomes zero or negative then relative convergence has been achieved.

To compute the absolute convergence the following criteria is chosen. After each iteration the sum of the pressures are computed. Let the result for the k'th iteration be denoted:

$$(10) \quad y_k = \sum_i \sum_j P_{i,j}^{(k)}$$

Assume that after infinitely many iterations this sum will be $y_{k\infty}$ and set:

$$y_k = y_{k\infty} - Ae^{-Bk} \quad (A \text{ and } B \text{ constants})$$

from which:

$$(11) \quad y_{k\infty} = y_k + \frac{(y_k - y_{k-1})^2}{2y_{k-1} - y_{k-2} - y_k}$$

$y_{k\infty}$ is calculated after each iteration (exceptions, see later) and the absolute convergence is computed from:

$$(12) \quad \frac{y_{k\infty} - y_k}{y_k} \delta_A = \Delta_A$$

where δ_A is given by the input. When Δ_A becomes zero or negative absolute convergence has been achieved.

In order to obtain complete convergence, both relative and absolute convergence must be satisfied. Equations (9), (11) and (12) are printed as output after each iteration. Equation (11) serves an additional purpose, namely to extrapolate the pressure distribution. When y_k becomes a smooth curve and starts to level

off then a new extrapolated pressure distribution is calculated from

$$(13) \quad P_{i,j} = \frac{y_{k\infty}}{y_k} \cdot P_{i,j}^{(k)}$$

and the pressure iterations proceed from this new distribution either until convergence is achieved or until y_k again becomes sufficiently smooth that Eq.(13) may be used once more.

It remains to define the criteria for "smoothness". As applied to Eq.(11) $y_{k\infty}$ is not calculated for the first 2 iterations or for the 2 iterations following a pressure extrapolation. In these cases the computer output shows:

$$(14) \quad \begin{aligned} y_{k\infty} &= 10^5 \\ \Delta_A &= 1.0 \end{aligned}$$

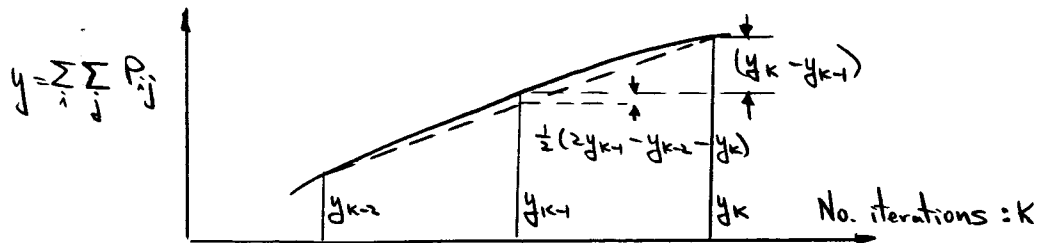
Furthermore $y_{k\infty}$ is not calculated if the y_k -curve is not monotonely increasing with decreasing gradient, i.e.:

$$(15) \quad \left. \begin{aligned} a) & (2y_{k-1} - y_{k-2} - y_k) > 0 \\ b) & (y_k - y_{k-1}) \leq 10^{-6} \cdot y_k \end{aligned} \right\} \begin{aligned} y_{k\infty} & \text{ by Eq.(11)} \\ \Delta_A & \text{ by Eq.(12)} \end{aligned}$$

$$(16) \quad \left. \begin{aligned} a) & k \leq 2, (k - k_{\text{extrapolation}}) \leq 2 \\ b) & (2y_{k-1} - y_{k-2} - y_k) < 0 \\ c) & (2y_{k-1} - y_{k-2} - y_k) = 0, (y_k - y_{k-1}) \neq 0 \\ d) & (2y_{k-1} - y_{k-2} - y_k) > 0, (y_k - y_{k-1}) \leq 0 \end{aligned} \right\} \begin{aligned} y_{k\infty} &= 10^6 \\ \Delta_A &= 1.0 \end{aligned}$$

$$(17) \quad \left. \begin{aligned} a) & (2y_{k-1} - y_{k-2} - y_k) = 0, (y_k - y_{k-1}) = 0 \\ b) & (2y_{k-1} - y_{k-2} - y_k) > 0, 0 < (y_k - y_{k-1}) \leq 10^{-6} \cdot y_k \end{aligned} \right\} \begin{aligned} y_{k\infty} &= y_k \\ \Delta_A &= 0.0 \end{aligned}$$

Graphically:



Similarly, Eq.(13) is not applied until $y_{k\infty}$ is "smooth". Basically this is determined by the input item δ_{ex} which specifies how small the relative difference between two consecutive $y_{k\infty}$ must be for extrapolation to be performed. In addition the $y_{k\infty}$ -curve must be increasing. Hence, the criteria for extrapolation becomes:

$$\begin{array}{lcl}
 (18) & \left. \begin{array}{l}
 \text{a) } 0 \leq \left(\frac{y_{k-1,\infty} - y_{k-2,\infty}}{y_{k-1,\infty}} \right) \leq \delta_{ex} \\
 \text{b) } 0 \leq \left(\frac{y_{k\infty} - y_{k-1,\infty}}{y_{k\infty}} \right) \leq \delta_{ex} \\
 \text{c) } \Delta_A \neq 1.0 \\
 \text{d) } k \geq 4, (k - k_{\text{extrapolation}}) \geq 4
 \end{array} \right\} & \begin{array}{l}
 \text{When these equations are} \\
 \text{satisfied Eq. (13) is} \\
 \text{performed, otherwise not.}
 \end{array}
 \end{array}$$

NOMENCLATURE FOR APPENDIX A

C	Radial clearance, inch
D	Journal diameter, Inch
F	Force, lbs.
\bar{F}	Dimensionless Frictional Force
f	Friction coefficient = F/W
f_r, f_t	Radial and tangential force components, dimensionless, see Fig. 2.
f_v, f_h	Vertical and horizontal force components, dimensionless, see Fig. 2.
h	Dimensionless film thickness
i, j	Finite difference coordinates, axial and circumferential
k	Iteration number
L	Bearing length, inch
m	Number of circumferential subdivisions
n	Number of axial subdivisions
N	Journal speed, RPS
P	Dimensionless pressure (above ambient)
Q_x, Q_z	Flow in x, z direction
R	Journal radius, inch
S	Sommerfeld number
t	Time, seconds
x, z	Circumferential and axial coordinates, dimensionless
y_k	Sum of all pressures after the k'th iteration, see Eq.(10)
y_{koo}	Extrapolated pressure sum after the k'th iteration, see Eq.(11)
α	Attitude angle, degrees
$\dot{\alpha}$	Tangential speed of journal center, rad/sec.
δ_A	Absolute convergence limit, see Eq. (12)
δ_R	Relative convergence limit, see Eq. (9)
Δ_A	Error in absolute convergence, see Eq. (12)
Δ_R	Error in relative convergence, see Eq. (9)
ϵ	Eccentricity ratio
$\dot{\epsilon}$	Radial speed of journal center, sec^{-1}
θ	Circumferential angular coordinate, See Fig. 2
μ	Viscosity, lbs-sec/in^2
ω	Angular speed of journal, rad/sec.

APPENDIX B

DYNAMIC LOAD ANALYSIS OF THE TILTING PAD BEARING

Steady State Equilibrium

Referring to Fig. B-1, let the center of the tilting pad bearing be O_B . The bearing is made up of a number of tilting pads, the arbitrary pad having the pivot point P located in an angle ψ from the vertical load line. The pad is free to tilt around the pivot point which for convenience is assumed to be located on the surface of the pad. The steady state position of the journal center is O_J which is the origin of two fixed coordinate systems: the x - y -system (x -axis vertical downward, y -axis horizontal) and the ξ - η -system (the ξ -axis passing through the pivot point). The location of O_J with respect to the bearing center is given by the eccentricity $O_B O_J = e_o = C' \epsilon_o$ and the attitude angle ϕ_o . The steady state position of the pad center is designated O_n such that the journal center eccentricity with respect to the pad is determined by $O_n O_J = e = C \epsilon$. The corresponding attitude angle is ϕ . The journal radius is R , the radius of the pad is $O_n P = R + C$ and the radius of the circle passing through all pivot points with center in O_B is $O_B P = R + C'$.

The point O_{no} is the center of curvature of the pad with no tilting. Hence, $O_{no} O_n$ is a circular arc, or for small motions, a line perpendicular to $O_{no} P$. Projecting O_J on $O_{no} P$ yields:

$$(1) \quad \epsilon \cos \phi = 1 - \frac{C'}{C} - \frac{C'}{C} \epsilon_o \cos (\psi - \phi_o)$$

This equation contains three unknowns, namely ϵ , ϕ and ϕ_o since ϵ_o is the independent variable. The second equation derives from the requirement that the force on the pad passes through the pivot point which establishes a relationship between ϵ and ϕ (i.e. the journal center locus with respect to the pad). The third relationship is the requirement that the total horizontal force component (in the y -direction), summed over all pads, is zero:

$$(2) \quad \sum_{\text{all pads}} F \sin \psi = 0$$

Eq. (2) is usually used to determine ϕ_0 by trial-and-error as follows: for a particular case ϵ_0 , $\frac{C'}{C}$ and ψ are known in Eq.(1). For several assumed values of ϕ_0 calculate $\epsilon \cos \phi$ for each pad, determine the pad forces F from available pad data and plot $\sum F \sin \psi$ as a function of ϕ_0 . The zero point determines the desired value of ϕ_0 .

This procedure is at best tedious. It becomes very complicated if the pivot point is not in the center of the pad in which case the pad force F can be a multivalued function of $\epsilon \cos \phi$. However, when the pivot points are located symmetrically with respect to the vertical load line through the bearing center O_B then $\phi_0 = 0$. A further simplification arises when the pivot point is in the center of the pad since the pad force F then is uniquely determined by $\epsilon \cos \phi$. The analysis requires only that ϵ and ϕ are known for each pad. How these values have been arrived at is immaterial in so far as the analysis is concerned.

Fixed Pad Coefficients

In order to determine the spring and damping coefficients for the complete tilting pad bearing it is necessary to know the forces and their derivatives for each pad as if the pad was fixed. Under steady state conditions the journal center has the eccentricity ratio ϵ and the attitude angle ϕ with respect to the pad center. The fluid film pad force has the components F_ξ and F_η and under steady state conditions the resultant force passes through the pivot point, i.e. $F_\xi = -F$ and $F_\eta = 0$, see Fig. 1. Thus F denotes the load on the pad. Usually, the force is resolved along the radial and the tangential directions with the components F_r and F_t , respectively, see Fig.1. Hence:

$$(3) \quad \begin{Bmatrix} F_\xi \\ F_\eta \end{Bmatrix} = \begin{Bmatrix} -F \\ 0 \end{Bmatrix} = - \begin{Bmatrix} \cos \phi & \sin \phi \\ \sin \phi & -\cos \phi \end{Bmatrix} \begin{Bmatrix} F_r \\ F_t \end{Bmatrix}$$

For infinitesimally small motion around the steady state position the dynamic forces become from Eq.(3):

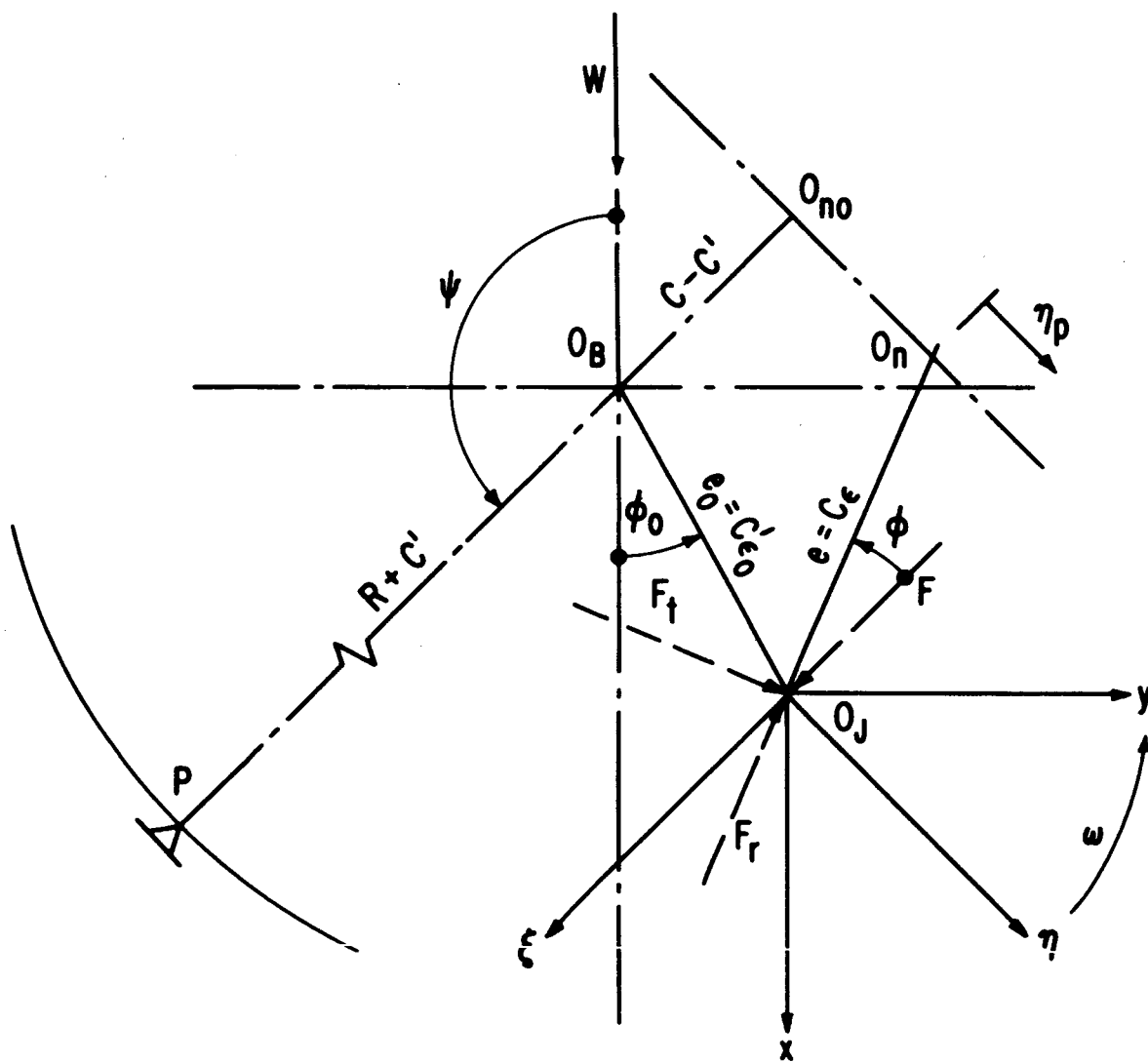


Fig. B 1 Coordinate System for Analysis

$$(4) \quad \begin{Bmatrix} dF_{\xi} \\ dF_{\eta} \end{Bmatrix} = \begin{Bmatrix} \cos\phi & \sin\phi \\ \sin\phi & -\cos\phi \end{Bmatrix} \begin{Bmatrix} dF_r + F_t d\phi \\ dF_t + F_r d\phi \end{Bmatrix}$$

The infinitesimal dynamic motion of the journal center is described by the coordinates (ξ, η) :

$$\xi = d(e \cos\phi) \quad \eta = d(e \sin\phi)$$

or

$$(5) \quad \begin{Bmatrix} de \\ e d\phi \end{Bmatrix} = \begin{Bmatrix} \cos\phi & \sin\phi \\ -\sin\phi & \cos\phi \end{Bmatrix} \begin{Bmatrix} \xi \\ \eta \end{Bmatrix}$$

The velocities transform similarly:

$$(6) \quad \begin{Bmatrix} d\dot{e} \\ e d\dot{\phi} \end{Bmatrix} = \begin{Bmatrix} \cos\phi & \sin\phi \\ -\sin\phi & \cos\phi \end{Bmatrix} \begin{Bmatrix} \dot{\xi} \\ \dot{\eta} \end{Bmatrix}$$

The dynamic force components dF_r and dF_t may be expressed in terms of the dynamic amplitudes. From Reynolds equation it can be shown that the fluid film force F can be written (Refs. 11, 13):

$$(7) \quad F = \lambda \omega (1 - 2 \frac{\dot{\phi}}{\omega}) \cdot f(\epsilon, \phi, \frac{\dot{\epsilon}}{\omega} / (1 - 2 \frac{\dot{\phi}}{\omega}))$$

where:

$$(8) \quad \lambda = \frac{\mu R L}{\pi} \left(\frac{R}{C}\right)^2$$

$$(9) \quad F = \frac{1}{S_P}$$

$$(10) \quad S_P = \frac{\mu N D L}{F} \left(\frac{R}{C}\right)^2 \quad (\text{Pad Sommerfeld Number})$$

Therefore:

(11)

$$dF = \lambda \omega \left\{ (1 - 2 \frac{\dot{\phi}}{\omega}) \left[\frac{\partial f}{\partial \epsilon} d\epsilon + \frac{\partial f}{\partial \phi} e d\phi + \frac{\partial f}{\partial (\frac{\dot{\epsilon}}{\omega})} d \left(\frac{\dot{\epsilon}}{\omega} / (1 - 2 \frac{\dot{\phi}}{\omega}) \right) \right] - \frac{2f}{\omega \epsilon} e d\dot{\phi} \right\}$$

Now:

$$d\left(\frac{\dot{\epsilon}/\omega}{1-2\dot{\phi}/\omega}\right) = \frac{1}{1-2\dot{\phi}/\omega} d(\dot{\epsilon}) + \frac{2(\dot{\epsilon}/\omega)}{(1-2\dot{\phi}/\omega)^2} d(\dot{\phi}/\omega) = d(\dot{\epsilon}/\omega)$$

because at the equilibrium position $\dot{\epsilon} = \dot{\phi} = 0$. Hence, Eq.(11) reduces to:

$$(12) \quad dF = \frac{1}{C} \lambda \omega \left\{ \frac{\partial f}{\partial \epsilon} d\epsilon + \frac{\partial f}{\epsilon \partial \phi} \epsilon d\phi + \frac{1}{\omega} \frac{\partial f}{\partial (\dot{\epsilon}/\omega)} d\dot{\epsilon} - \frac{1}{\omega} \frac{2f}{\epsilon} \epsilon d\dot{\phi} \right\}$$

Eq.(12) applies to both F_r and F_t . Let the corresponding dimensionless forces be denoted to f_r and f_t as defined by Eq.(7). Thus, by substitution of Eq.(12) into Eq.(4):

$$(13) \quad \begin{Bmatrix} dF_z \\ dF_\eta \end{Bmatrix} = -\frac{1}{C} \lambda \omega \begin{Bmatrix} \cos \phi & \sin \phi \\ \sin \phi & -\cos \phi \end{Bmatrix} \begin{Bmatrix} \frac{\partial f_r}{\partial \epsilon} & \left(\frac{\partial f_r}{\epsilon \partial \phi} + \frac{f_t}{\epsilon} \right) \\ \frac{\partial f_t}{\partial \epsilon} & \left(\frac{\partial f_t}{\epsilon \partial \phi} - \frac{f_r}{\epsilon} \right) \end{Bmatrix} \begin{Bmatrix} d\epsilon \\ d\phi \end{Bmatrix} + \frac{1}{\omega} \begin{Bmatrix} \frac{\partial f_r}{\partial (\dot{\epsilon}/\omega)} & -\frac{2f_r}{\epsilon} \\ \frac{\partial f_t}{\partial (\dot{\epsilon}/\omega)} & -\frac{2f_t}{\epsilon} \end{Bmatrix} \begin{Bmatrix} d\dot{\epsilon} \\ d\dot{\phi} \end{Bmatrix}$$

Define the fixed pads spring and damping coefficients by:

$$(14) \quad dF_z = -K_{zz} \xi - C_{zz} \dot{\xi} - K_{z\eta} \eta - C_{z\eta} \dot{\eta}$$

$$dF_\eta = -K_{\eta z} \xi - C_{\eta z} \dot{\xi} - K_{\eta\eta} \eta - C_{\eta\eta} \dot{\eta}$$

To determine the 8 coefficients, substitute Eq.(5) and (6) into Eq. (13) and collect the terms in accordance with Eq.(14) to get:

$$(15) \quad K_{zz} = \frac{1}{C} \lambda \omega \left[\frac{\partial f_r}{\partial \epsilon} \cos^2 \phi - \frac{\partial f_t}{\epsilon \partial \phi} \sin^2 \phi - \left(\frac{\partial f_r}{\epsilon \partial \phi} - \frac{\partial f_t}{\partial \epsilon} \right) \cos \phi \sin \phi - \frac{f_t}{\epsilon} \sin \phi \right]$$

$$(16) \quad \omega C_{zz} = \frac{1}{C} \lambda \omega \left[\frac{\partial f_r}{\partial (\dot{\epsilon}/\omega)} \cos^2 \phi + \frac{\partial f_t}{\partial (\dot{\epsilon}/\omega)} \cos \phi \sin \phi - \frac{2f_t}{\epsilon} \sin \phi \right]$$

$$(17) \quad K_{z\eta} = \frac{1}{C} \lambda \omega \left[\frac{\partial f_r}{\epsilon \partial \phi} \cos^2 \phi + \frac{\partial f_t}{\partial \epsilon} \sin^2 \phi + \left(\frac{\partial f_t}{\epsilon \partial \phi} + \frac{\partial f_r}{\partial \epsilon} \right) \cos \phi \sin \phi + \frac{f_r}{\epsilon} \cos \phi \right]$$

$$(18) \quad \omega C_{z\eta} = \frac{1}{C} \lambda \omega \left[\frac{\partial f_t}{\partial (\dot{\epsilon}/\omega)} \sin^2 \phi + \frac{\partial f_r}{\partial (\dot{\epsilon}/\omega)} \cos \phi \sin \phi + \frac{2f_r}{\epsilon} \cos \phi \right]$$

$$(19) \quad K_{\eta z} = \frac{1}{C} \lambda \omega \left[-\frac{\partial f_t}{\partial \epsilon} \cos^2 \phi - \frac{\partial f_r}{\epsilon \partial \phi} \sin^2 \phi + \left(\frac{\partial f_t}{\epsilon \partial \phi} + \frac{\partial f_r}{\partial \epsilon} \right) \cos \phi \sin \phi + \frac{f_r}{\epsilon} \sin \phi \right]$$

$$(20) \quad \omega C_{\eta z} = \frac{1}{C} \lambda \omega \left[-\frac{\partial f_t}{\partial (\dot{\epsilon}/\omega)} \cos^2 \phi + \frac{\partial f_r}{\partial (\dot{\epsilon}/\omega)} \cos \phi \sin \phi - \frac{2f_r}{\epsilon} \sin \phi \right]$$

$$(21) \quad K_{\eta\eta} = \frac{1}{C} \lambda \omega \left[-\frac{\partial f_k}{\partial \phi} \cos^2 \phi + \frac{\partial f_r}{\partial \epsilon} \sin^2 \phi + \left(\frac{\partial f_r}{\partial \phi} - \frac{\partial f_k}{\partial \epsilon} \right) \cos \phi \sin \phi - \frac{f_z}{\epsilon} \cos \phi \right]$$

$$(22) \quad \omega C_{\eta\eta} = \frac{1}{C} \lambda \omega \left[\frac{\partial f_r}{\partial (\epsilon(\omega))} \sin^2 \phi - \frac{\partial f_k}{\partial (\epsilon(\omega))} \cos \phi \sin \phi + \frac{\partial f_z}{\partial \epsilon} \cos \phi \right]$$

where:

$$(23) \quad f_\xi = \frac{-1}{s_p}$$

$$(24) \quad f_\eta = 0$$

$$(25) \quad \frac{1}{C} \lambda \omega = \frac{1}{C} F S_p$$

and all forces and derivatives are calculated for the given steady state position, defined by ϵ .

Tilting Pad Coefficients

Referring to Fig. B1, O_n is the steady state position of the pad center. Under dynamic load the pad center oscillates around O_n with the amplitude η_p such that η_p/R_p represents the dynamic tilting angle of the pad (R_p is the distance from the actual pad pivot to the pad center). The moment on the pad from the fluid film pressure is $-R_p dF_\eta$. Therefore, if the mass moment of inertia of the pad is I the equation of motion becomes:

$$I \frac{\ddot{\eta}_p}{R_p} = -R_p dF_\eta$$

or

$$(26) \quad \frac{I}{R_p^2} \ddot{\eta}_p = M \ddot{\eta}_p = -dF_\eta$$

where:

$$(27) \quad M = \frac{I}{R_p^2}$$

Thus, under dynamic conditions η should be replaced by $(\eta - \eta_p)$ in Eq. (14). In order to eliminate η_p substitute the expression for dF_η into Eq. (26):

$$(28) \quad M\ddot{\eta}_p = K_{\eta\xi}\xi + C_{\eta\xi}\dot{\xi} + K_{\eta\eta}(\eta - \eta_p) + C_{\eta\eta}(\dot{\eta} - \dot{\eta}_p)$$

Let the dynamic motion of the journal center around the steady state position be harmonic:

$$(29) \quad (\xi, \eta) e^{i\omega t}$$

Hence, solve Eq. (28):

$$(30) \quad \eta - \eta_p = -\frac{(K_{\eta\xi} + i\omega C_{\eta\xi})\xi + M\omega^2\eta}{K_{\eta\eta} - M\omega^2 + i\omega C_{\eta\eta}} = -[(K_{\eta\xi} + i\omega C_{\eta\xi})\xi + M\omega^2\eta] (P - iQ)$$

where:

$$(31) \quad P = \frac{K_{\eta\eta} - M\omega^2}{(K_{\eta\eta} - M\omega^2)^2 + (\omega C_{\eta\eta})^2}$$

$$(32) \quad Q = \frac{\omega C_{\eta\eta}}{(K_{\eta\eta} - M\omega^2)^2 + (\omega C_{\eta\eta})^2}$$

Thus, replacing η by $(\eta - \eta_p)$ Eq. (14) becomes:

$$(33) \quad \begin{aligned} dF_\xi &= -(K'_{\xi\xi} + i\omega C'_{\xi\xi})\xi - (K'_{\xi\eta} + i\omega C'_{\xi\eta})\eta \\ dF_\eta &= (K'_{\eta\xi} + i\omega C'_{\eta\xi})\xi - (K'_{\eta\eta} + i\omega C'_{\eta\eta})\eta \end{aligned}$$

where $K'_{\xi\xi}$, $C'_{\xi\xi}$ etc., are the spring and damping coefficients for the tilting pad and given by:

$$(34) \quad K'_{\xi\xi} = K_{\xi\xi} - (PK_{\xi\eta} + Q\omega C_{\xi\eta})K_{\eta\xi} - (QK_{\xi\eta} - P\omega C_{\xi\eta})\omega C_{\eta\xi}$$

$$(35) \quad \omega C'_{\xi\xi} = \omega C_{\xi\xi} - (PK_{\xi\eta} + Q\omega C_{\xi\eta})\omega C_{\eta\xi} + (QK_{\xi\eta} - P\omega C_{\xi\eta})K_{\eta\xi}$$

$$(36) \quad K'_{\xi\eta} = -M\omega^2 (PK_{\xi\eta} + Q\omega C_{\xi\eta})$$

$$(37) \quad \omega C'_{\xi\eta} = M\omega^2 (QK_{\xi\eta} - P\omega C_{\xi\eta})$$

$$(38) \quad K'_{\eta\xi} = -M\omega^2 (PK_{\eta\xi} + Q\omega C_{\eta\xi})$$

$$(39) \quad \omega C'_{\eta\xi} = M\omega^2 (QK_{\eta\xi} - P\omega C_{\eta\xi})$$

$$(40) \quad K'_{\eta\eta} = -M\omega^2 (PK_{\eta\eta} + Q\omega C_{\eta\eta}) = -M\omega^2 (1 + PM\omega^2)$$

$$(41) \quad \omega C'_{\eta\eta} = M\omega^2 (QK_{\eta\eta} - P\omega C_{\eta\eta}) = (M\omega^2)^2 Q$$

If the pad has no inertia, i.e. $M=0$, only $K'_{\xi\xi}$ and $\omega C'_{\xi\xi}$ remain as would be expected.

Bearing Spring and Damping Coefficients

Having determined the spring and damping coefficients for the individual tilting pads it remains to combine them into the overall bearing coefficients. The coordinate system for the bearing is the x-y-system, see Fig. B1, with the coordinate transformation:

$$(42) \quad \begin{Bmatrix} \xi \\ \eta \end{Bmatrix} = - \begin{Bmatrix} \cos\psi & \sin\psi \\ -\sin\psi & \cos\psi \end{Bmatrix} \begin{Bmatrix} x \\ y \end{Bmatrix}$$

$$(43) \quad \begin{Bmatrix} dF_x \\ dF_y \end{Bmatrix} = - \begin{Bmatrix} \cos\psi & -\sin\psi \\ \sin\psi & \cos\psi \end{Bmatrix} \begin{Bmatrix} dF_\xi \\ dF_\eta \end{Bmatrix}$$

where dF_x and dF_y are the dynamic forces measured in the x-y-system. The bearing spring and damping coefficients are defined by:

$$(44) \quad \begin{aligned} dF_x &= -K_{xx}\dot{x} - C_{xx}\dot{\dot{x}} - K_{xy}\dot{y} - C_{xy}\dot{\dot{y}} \\ dF_y &= -K_{yx}\dot{y} - C_{yx}\dot{\dot{y}} - K_{yy}\dot{x} - C_{yy}\dot{\dot{x}} \end{aligned}$$

Thus, substituting Eq.(42) and (43) into Eq. (33) and grouping terms in accordance with Eq.(44) yields:

$$(45) \quad K_{xx} = K'_{\xi\xi} \cos^2\psi + K'_{\eta\eta} \sin^2\psi - (K'_{\xi\eta} + K'_{\eta\xi}) \cos\psi \sin\psi$$

$$(46) \quad \omega C_{xx} = \omega C'_{\xi\xi} \cos^2\psi + \omega C'_{\eta\eta} \sin^2\psi - (\omega C'_{\xi\eta} + \omega C'_{\eta\xi}) \cos\psi \sin\psi$$

$$(47) \quad K_{xy} = K'_{\xi\eta} \cos^2\psi - K'_{\eta\xi} \sin^2\psi + (K'_{\xi\xi} - K'_{\eta\eta}) \cos\psi \sin\psi$$

$$(48) \quad \omega C_{xy} = \omega C'_{\xi\eta} \cos^2\psi - \omega C'_{\eta\xi} \sin^2\psi + (\omega C'_{\xi\xi} - \omega C'_{\eta\eta}) \cos\psi \sin\psi$$

$$(49) \quad K_{yx} = K'_{\eta\xi} \cos^2\psi - K'_{\xi\eta} \sin^2\psi + (K'_{\xi\xi} - K'_{\eta\eta}) \cos\psi \sin\psi$$

$$(50) \quad \omega C_{yx} = \omega C'_{\eta\xi} \cos^2\psi - \omega C'_{\xi\eta} \sin^2\psi + (\omega C'_{\xi\xi} - \omega C'_{\eta\eta}) \cos\psi \sin\psi$$

$$(51) \quad K_{yy} = K'_{\eta\eta} \cos^2\psi + K'_{\xi\xi} \sin^2\psi + (K'_{\xi\eta} + K'_{\eta\xi}) \cos\psi \sin\psi$$

$$(52) \quad \omega C_{yy} = \omega C'_{\eta\eta} \cos^2\psi + \omega C'_{\xi\xi} \sin^2\psi + (\omega C'_{\xi\eta} + \omega C'_{\eta\xi}) \cos\psi \sin\psi$$

A summation over all the pads making up the bearing gives the bearing spring and damping coefficients. If the pads have no inertia the equations simplify to:

$$(54) \quad \begin{aligned} K_{xx} &= K'_{\xi\xi} \cos^2\psi & \omega C_{xx} &= \omega C'_{\xi\xi} \cos^2\psi \\ K_{xy} &= K_{yx} = K'_{\xi\xi} \cos\psi \sin\psi & \omega C_{xy} &= \omega C_{yx} = \omega C'_{\xi\xi} \cos\psi \sin\psi \\ K_{yy} &= K'_{\xi\xi} \sin^2\psi & \omega C_{yy} &= \omega C'_{\xi\xi} \sin^2\psi \end{aligned}$$

Thus, for symmetry around the x-axis and no pad inertia, the cross-coupling terms disappear.

Pad Motion

The pad motion is given by Eq.(30) which can also be written:

$$(55) \quad \eta_p = \frac{(K_{\eta\xi} + i\omega C_{\eta\xi})\xi + (K_{\eta\eta} + i\omega C_{\eta\eta})\eta}{K_{\eta\eta} - M\omega^2 + i\omega C_{\eta\eta}}$$

Let $\eta_o = \eta_p$ for $M = 0$, i.e. for no pad inertia:

$$(56) \quad \eta_o = \eta + \frac{K_{\eta\xi} + i\omega C_{\eta\xi}}{K_{\eta\eta} + i\omega C_{\eta\eta}} \xi$$

Then:

$$(57) \quad \frac{\eta_p}{\eta_o} = \frac{K_{\eta\eta} + i\omega C_{\eta\eta}}{K_{\eta\eta} - M\omega^2 + i\omega C_{\eta\eta}} = 1 + \frac{M\omega^2}{K_{\eta\eta} - M\omega^2 + i\omega C_{\eta\eta}} = 1 + PM\omega^2 - iQM\omega^2$$

or:

$$(58) \quad \left| \frac{\eta_p}{\eta_o} \right| = \sqrt{(1 + PM\omega^2)^2 + (QM\omega^2)^2}$$

$$(59) \quad \arg(\eta_o) - \arg(\eta_p) = \tan^{-1} \left(\frac{QM\omega^2}{1+PM\omega^2} \right) = \tan^{-1} \left(\frac{\omega C_{\eta\eta} M \omega^2}{K_{\eta\eta} (K_{\eta\eta} - M\omega^2) + (\omega C_{\eta\eta})^2} \right)$$

Eq.(58) gives the amplitude ratio, i.e. the magnification factor, and Eq. (59) gives the phase angle lag with respect to a inertialess pad. Thus the two equations indicate how well the pad follows the shaft motion. The phase angle becomes 90° when:

$$(60) \quad M_{crit} \omega^2 = \frac{K_{\eta\eta}^2 + (\omega C_{\eta\eta})^2}{K_{\eta\eta}}$$

Hence, if the pad mass satisfies Eq.(60) there will be a resonance of the pad motion.

It is convenient to use Eq.(60) to establish a value for M, designated the critical mass. In dimensionless form Eq. (60) may be written:

$$(61) \quad \frac{CWM_{crit}}{\left[\mu DL \left(\frac{R}{C} \right)^2 \right]^2} = \frac{1}{4\pi^2 S} \frac{\left(\frac{CK_{\eta\eta}}{W} \right)^2 + \left(\frac{C\omega C_{\eta\eta}}{W} \right)^2}{\frac{CK_{\eta\eta}}{W}}$$

where S is the bearing Sommerfeld number.

NOMENCLATURE FOR APPENDIX B

C	Pad clearance (radius of curvature of pad minus journal radius) inch.
C'	Pivot circle clearance (radius of pivot circle minus journal radius) in.
$C_{xx}, C_{xy}, C_{yx}, C_{yy}$	Bearing damping coefficients, lbs sec/in.
$C_{\xi\xi}, C_{\xi\eta}, C_{\eta\xi}, C_{\eta\eta}$	Fixed pad damping coefficients, lbs.sec/in.
$C'_{\xi\xi}, C'_{\xi\eta}, C'_{\eta\xi}, C'_{\eta\eta}$	Tilting pad damping coefficients, lbs.sec/in.
D	Journal diameter, inch
e	Journal center eccentricity with respect to pad center, inch.
e_o	Journal center eccentricity with respect to bearing center, inch.
F	Load on pad, lbs.
F_r, F_t	Radial and tangential components of pad load, lbs.
F_ξ, F_η	Components in ξ and η -direction of pad load, lbs. (see Fig.1)
f	$= F/\lambda\omega$, dimensionless pad force
f_r, f_t	Radial and tangential components of dimensionless pad force
f_ξ, f_η	Components in ξ and η -direction of dimensionless pad force
I	Transverse mass moment of inertia of shoe around pivot, lbs.in.sec ²
$K_{xx}, K_{xy}, K_{yx}, K_{yy}$	Bearing spring coefficients, lbs/in.
$K_{\xi\xi}, K_{\xi\eta}, K_{\eta\xi}, K_{\eta\eta}$	Fixed pad spring coefficients, lbs/in.
$K'_{\xi\xi}, K'_{\xi\eta}, K'_{\eta\xi}, K'_{\eta\eta}$	Tilting pad spring coefficients, lbs/in.
L	Bearing length, inch
M	$= I/R_p^2$, equivalent pad mass, lbs.sec ² /in.
M_{crit}	Value of equivalent of pad mass to cause pad motion resonance, lbs.sec ² /in
N	Rotational speed of journal, RPS
P, Q	Coefficients defined by Eqs.(31) and (32)
R	Journal radius, inch
R_p	Radius from pad center to actual pivot point of pad, inch

S	$= (\mu NDL/W) \cdot (R/C)^2$, bearing Sommerfeld number
S_p	$= (\mu NDL/F) \cdot (R/C)^2$, pad Sommerfeld number
W	Bearing load, lbs.
x, y	Coordinates of journal center with respect to the bearing, see Fig. 1, inch.
ϵ	$= e/C$, eccentricity ratio with respect to the pad center
ϵ_o	$= e_o/C$, eccentricity ratio with respect to the bearing center
η_p	Amplitude for pad center motion, see Fig. 1 inch
η_o	Amplitude of the center of a massless pad, inch
λ	$= (\mu RL/\pi) \cdot (R/C)^2$ bearing coefficient
μ	Lubricant viscosity, lbs.sec/in ²
ξ, η	Coordinates of journal center with respect to the pad, see Fig. 1
ϕ	Attitude angle with respect to the pad load line, radians
ϕ_o	Attitude angle with respect to the bearing load line, radians
ψ	Angle from vertical (negative x-axis) to pad pivot point, see Fig. 1. inch
ω	Angular speed of shaft, radian/sec.

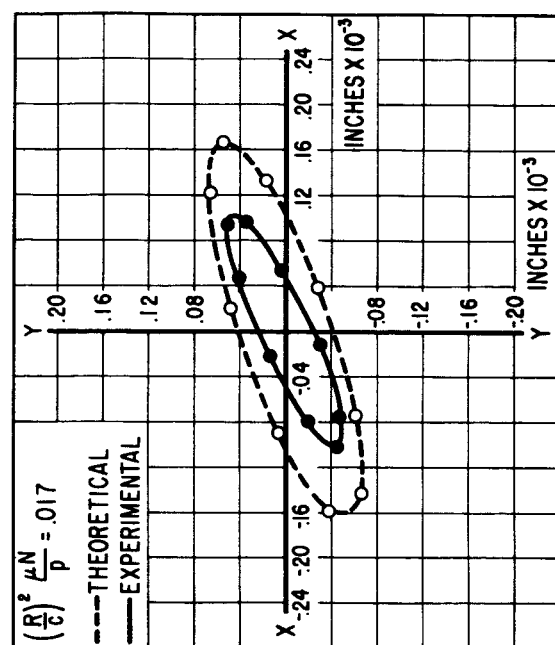
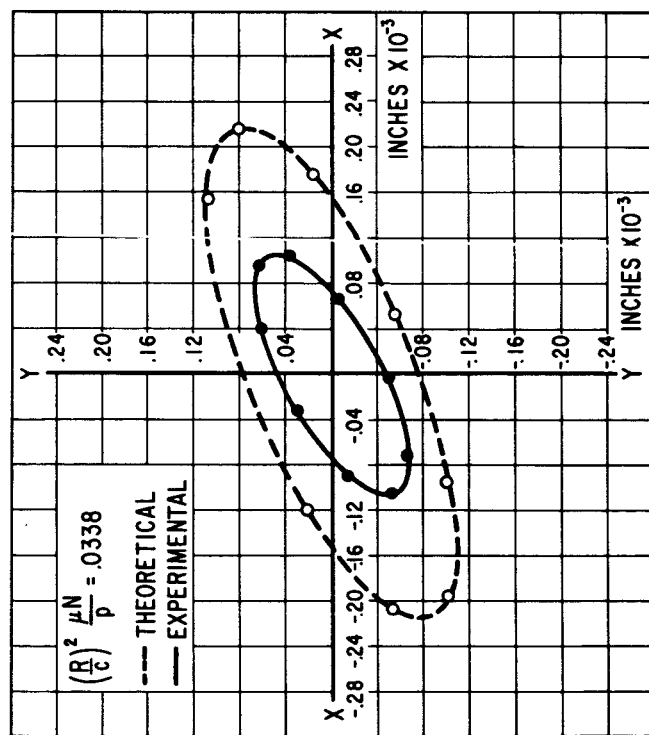
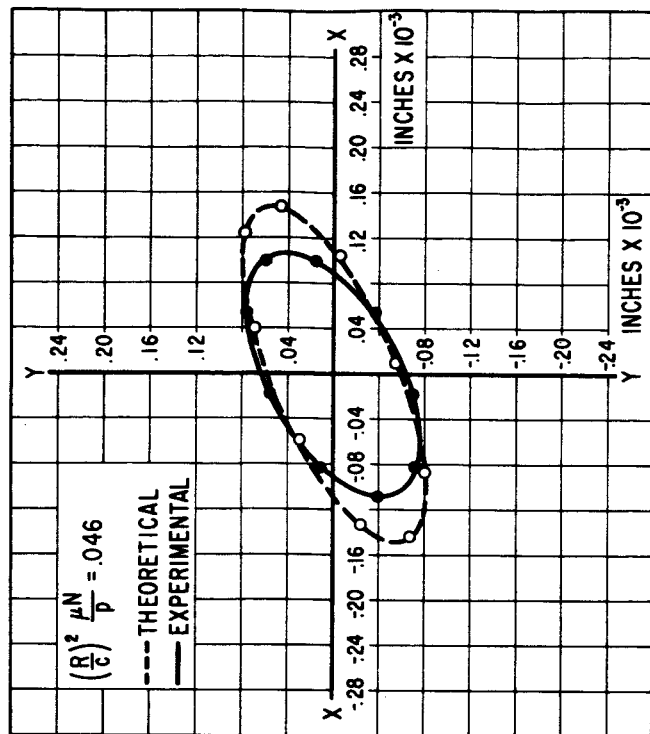
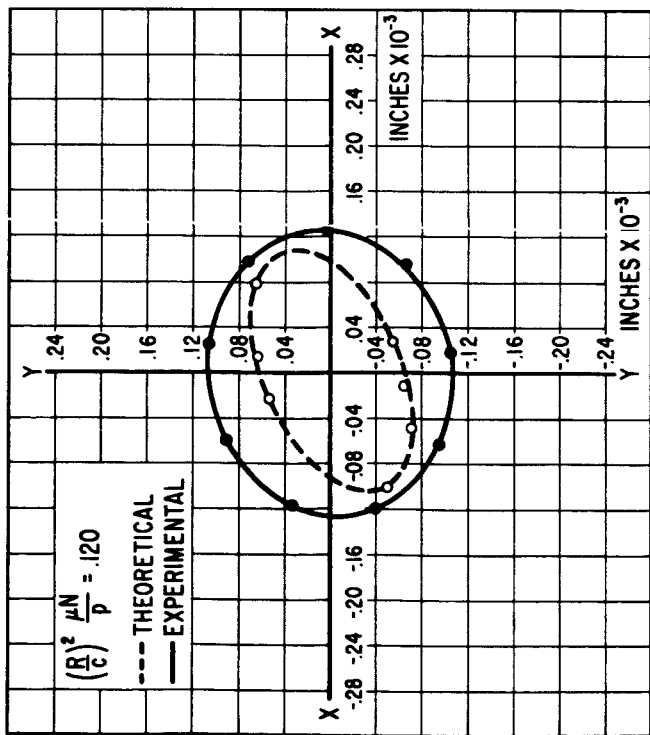


Fig. 1 Shaft Response Determined from Theory and by Experiment - From Ref. 1

$C/R = 4 \times 10^{-3}$ in/in., $\beta = 100^\circ$, $Re = 5820$

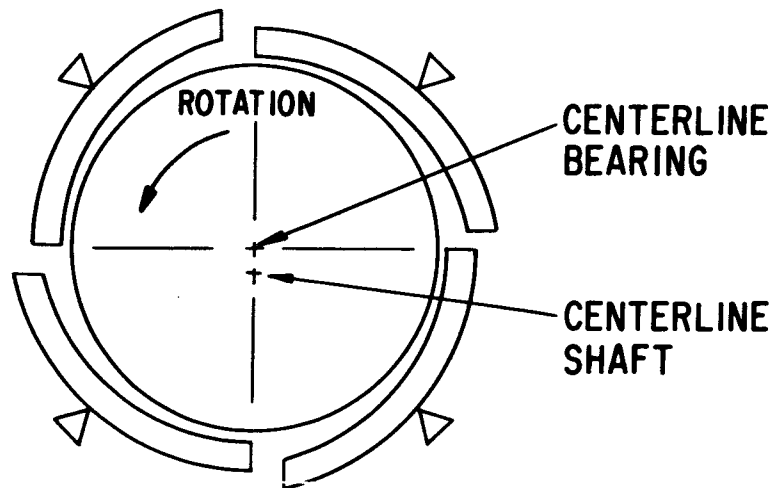
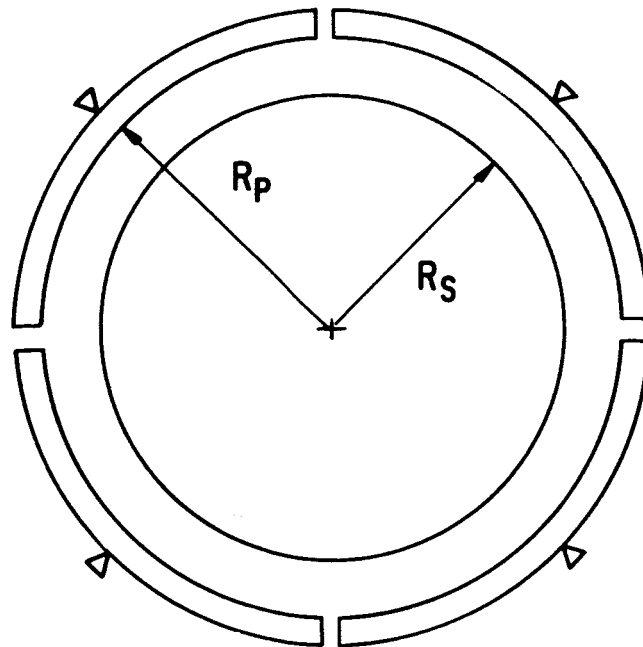
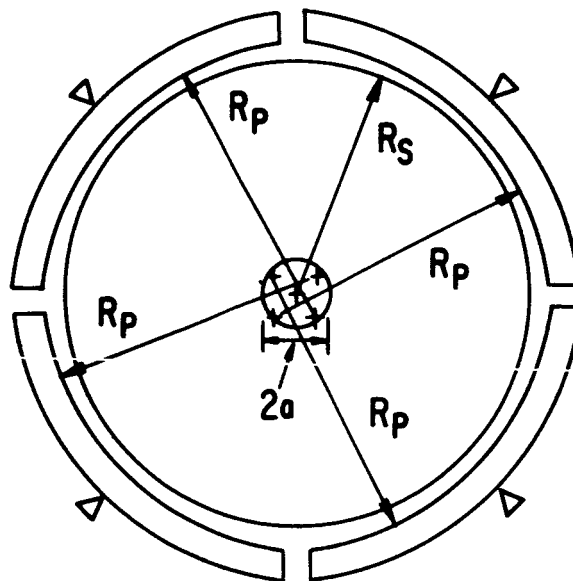


Fig. 2 Schematic of Tilting Pad Bearing.



4 PAD BEARING
ZERO PRELOAD
(a)



4 PAD BEARING
PRELOAD = a
(PRELOAD COEFFICIENT = $\frac{a}{R_p - R_s}$)
(b)

Fig. 3 Geometrical Arrangement of Pads

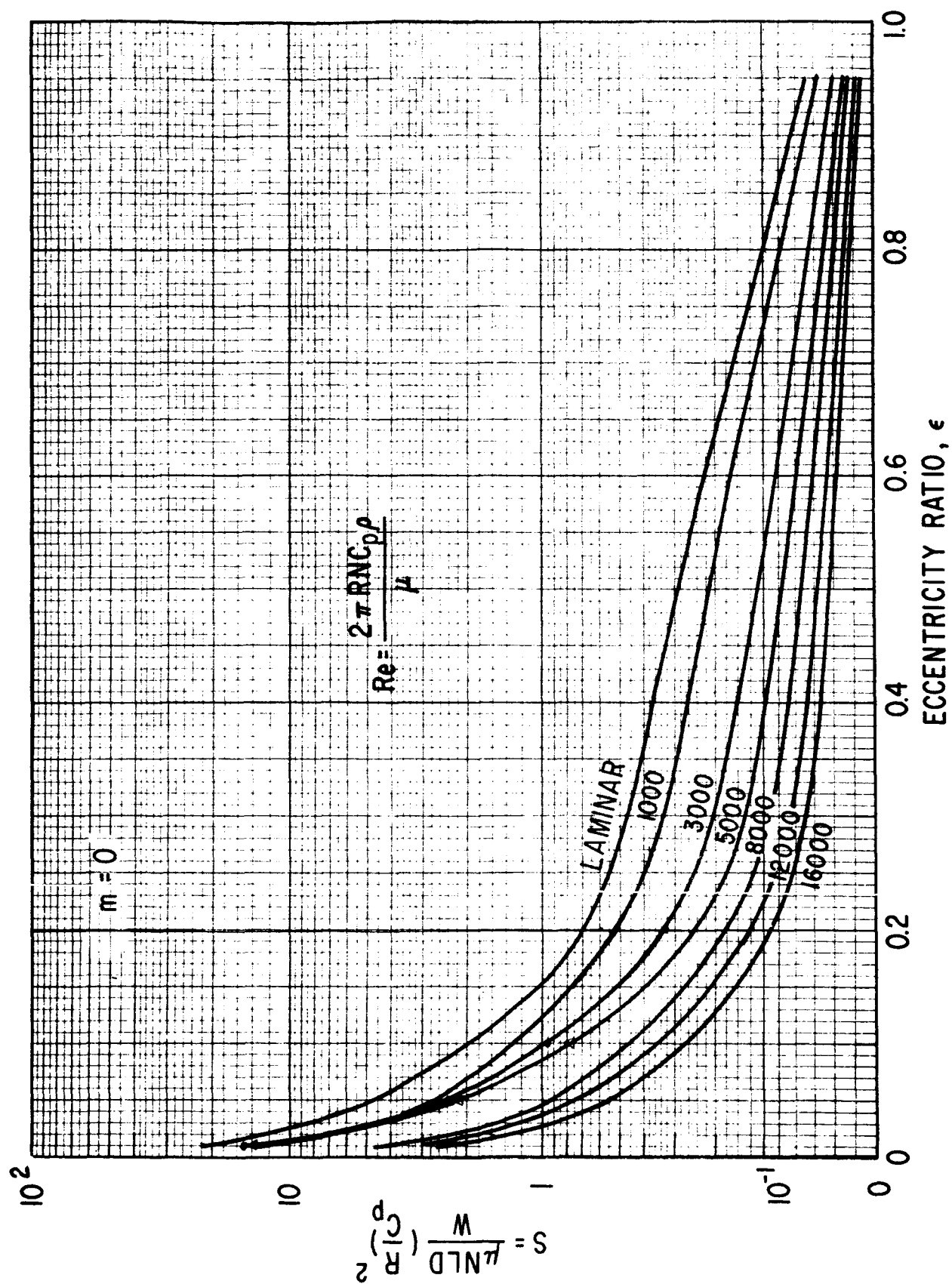


Fig. 4 Calculated Static Load Capacity - $m = 0$

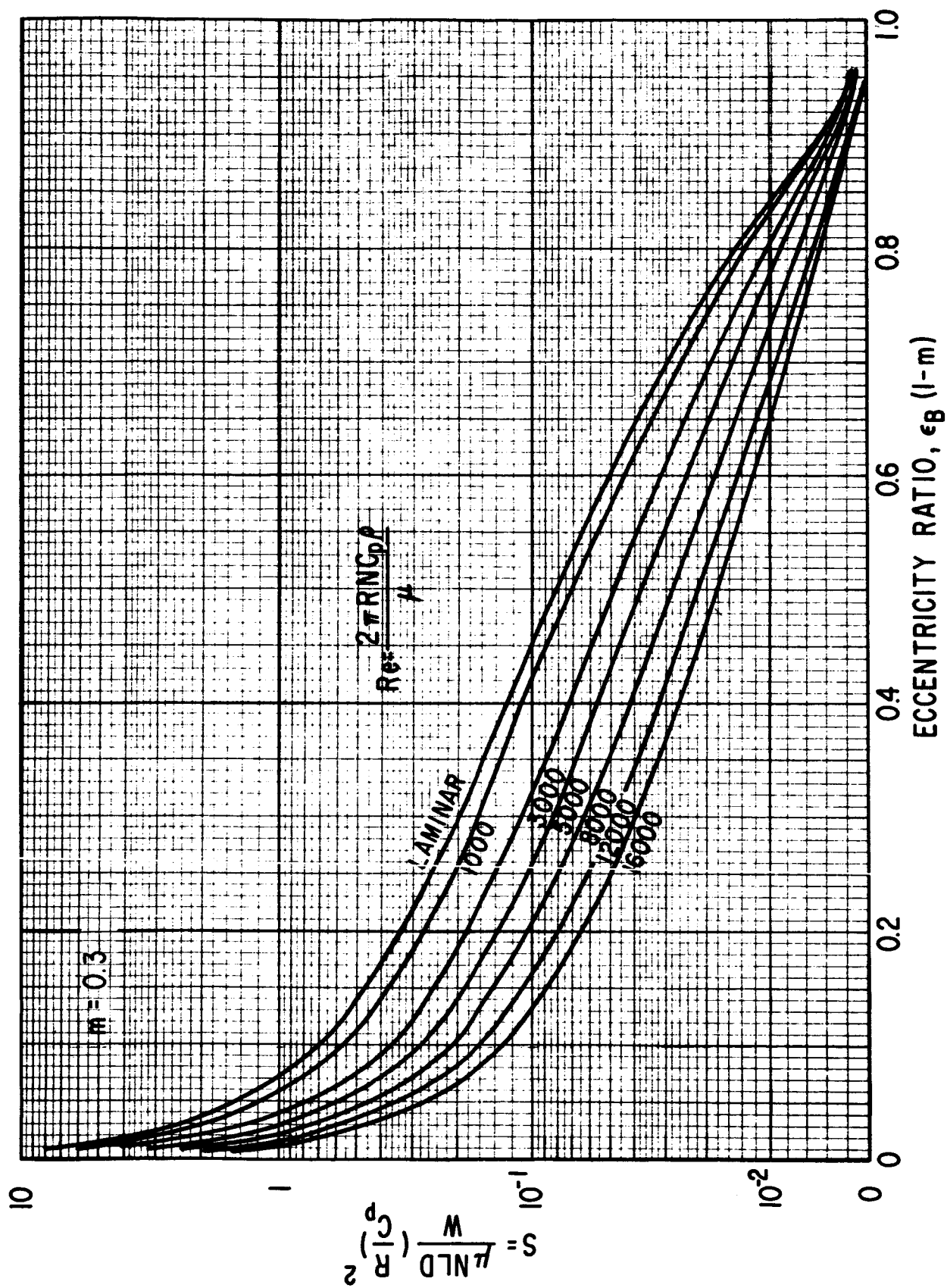


Fig. 5 Calculated Static Load Capacity - $m = 0.3$

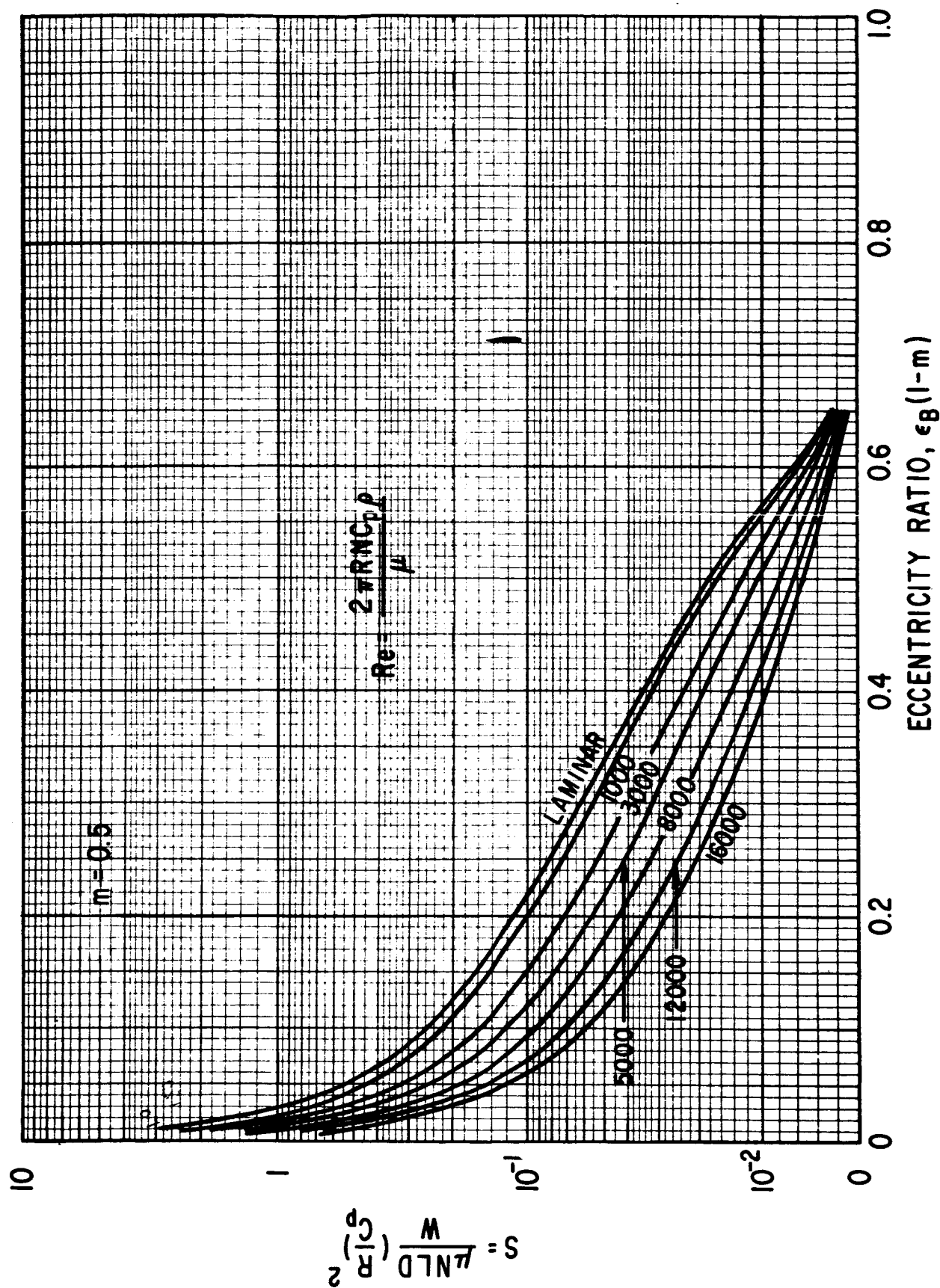


Fig. 6 Calculated Static Load Capacity - $m = 0.5$

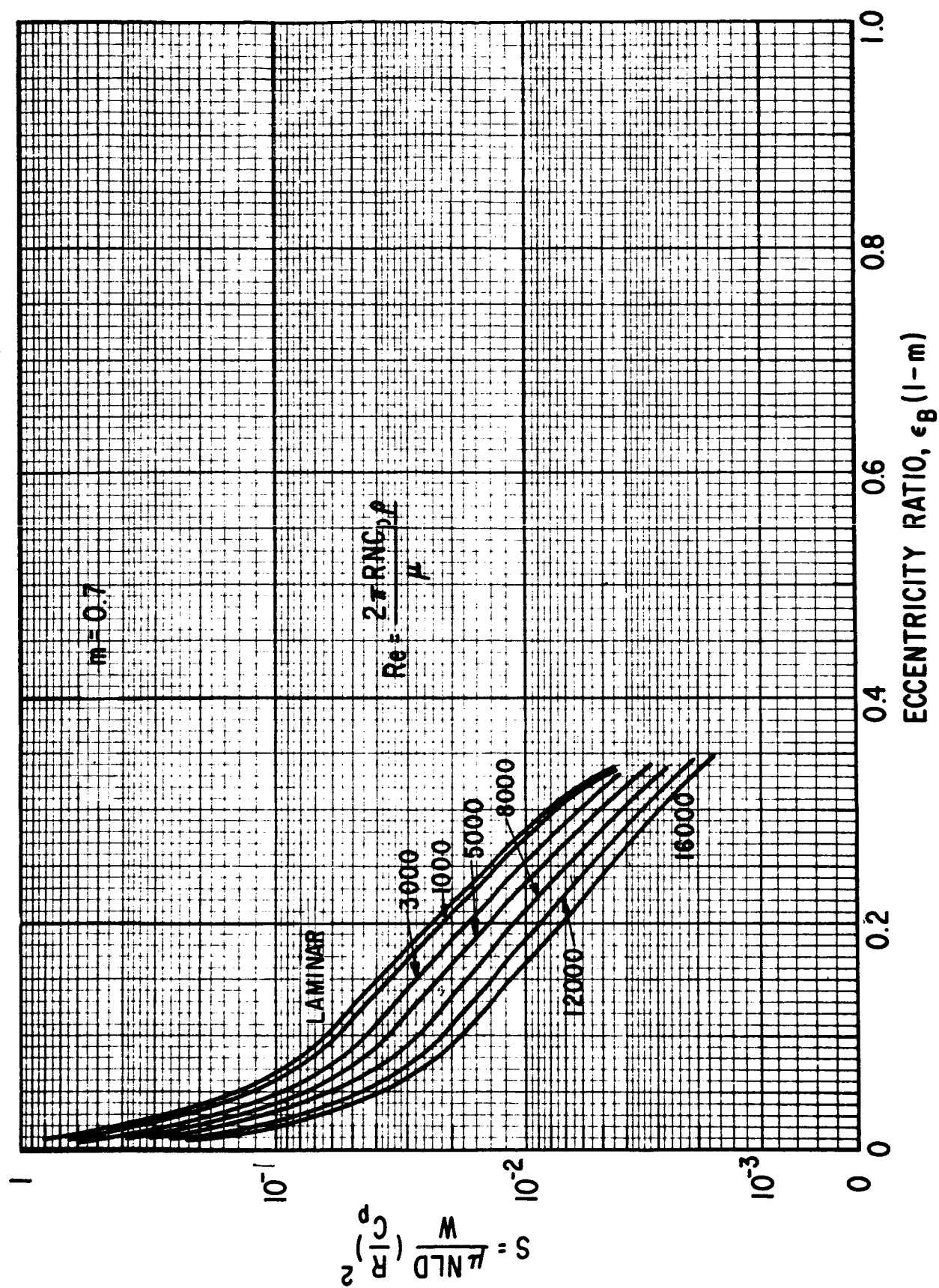


Fig. 7 Calculated Static Load Capacity - $m = 0.7$

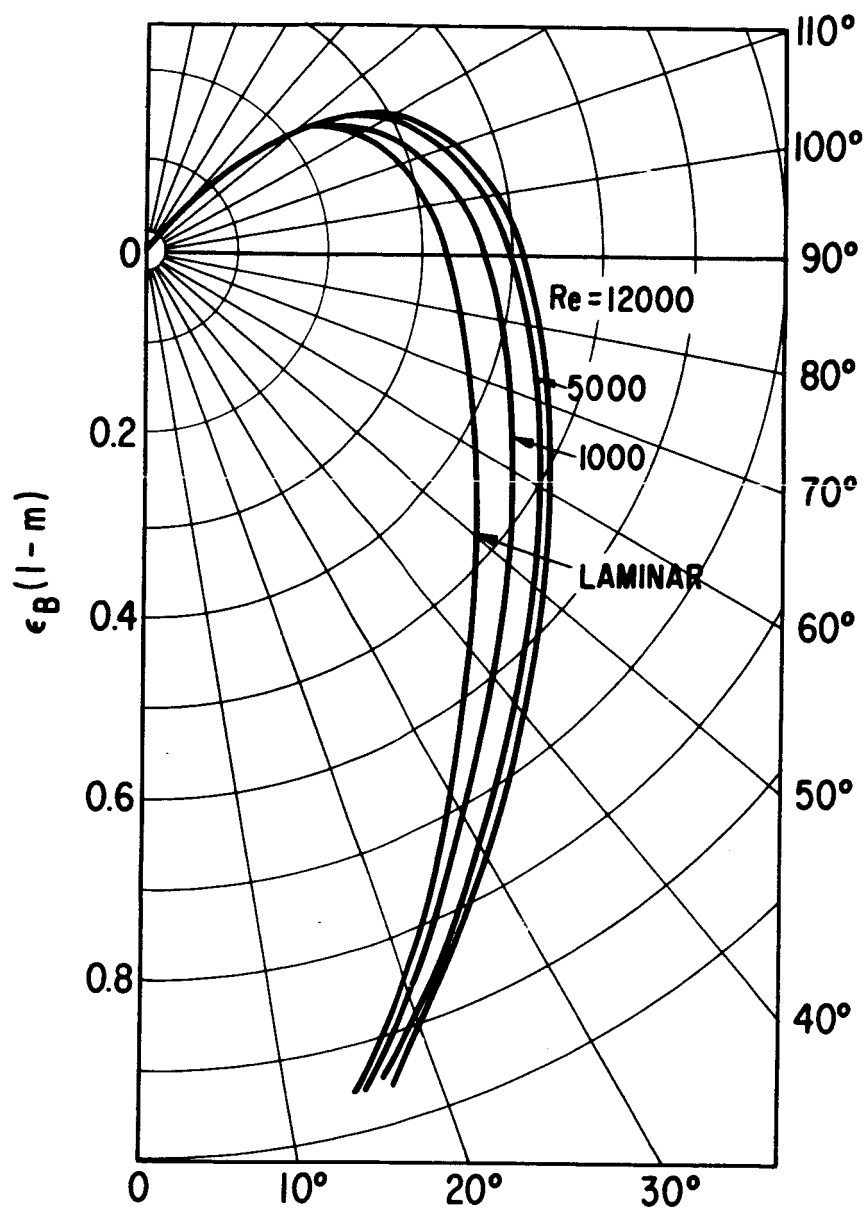


Fig. 8 Attitude Angle versus Eccentricity
for Single Pad
 $\beta = 80^\circ$
 $\theta_p = .55$

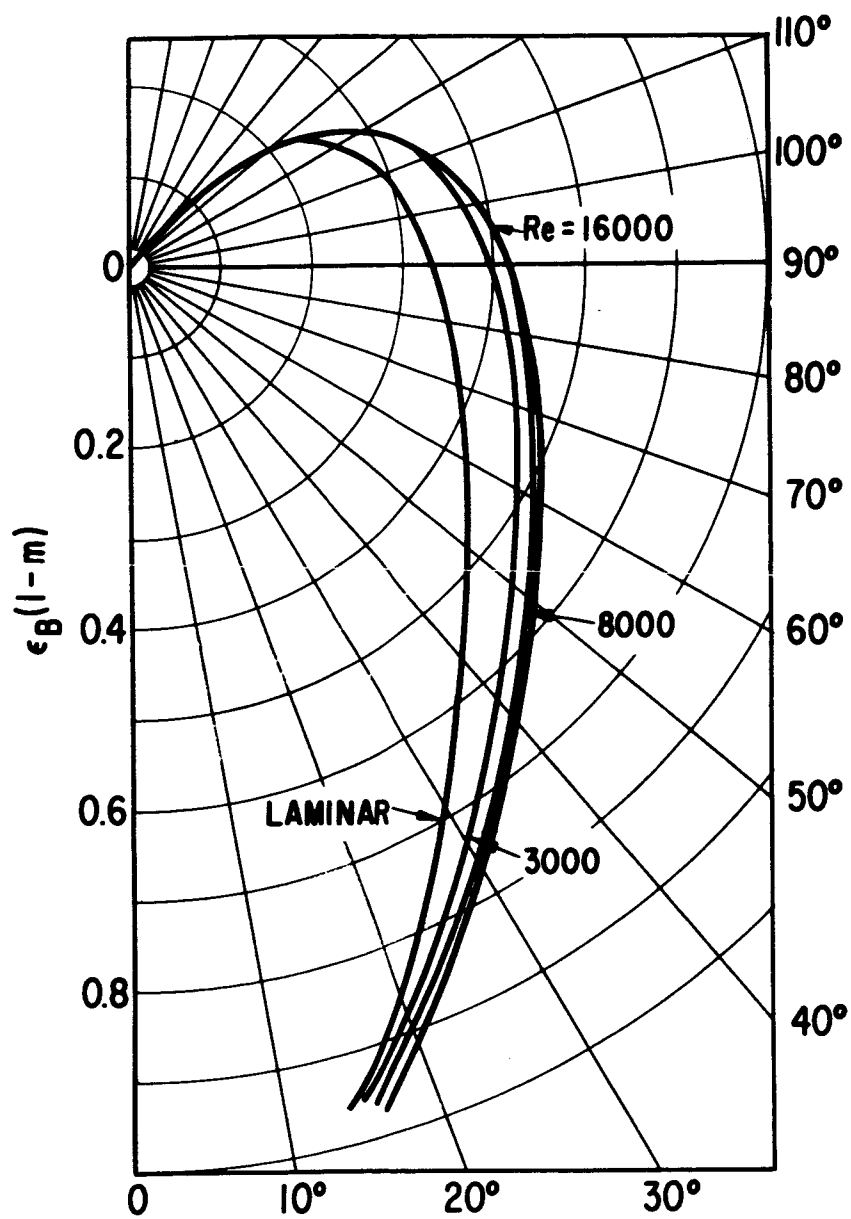
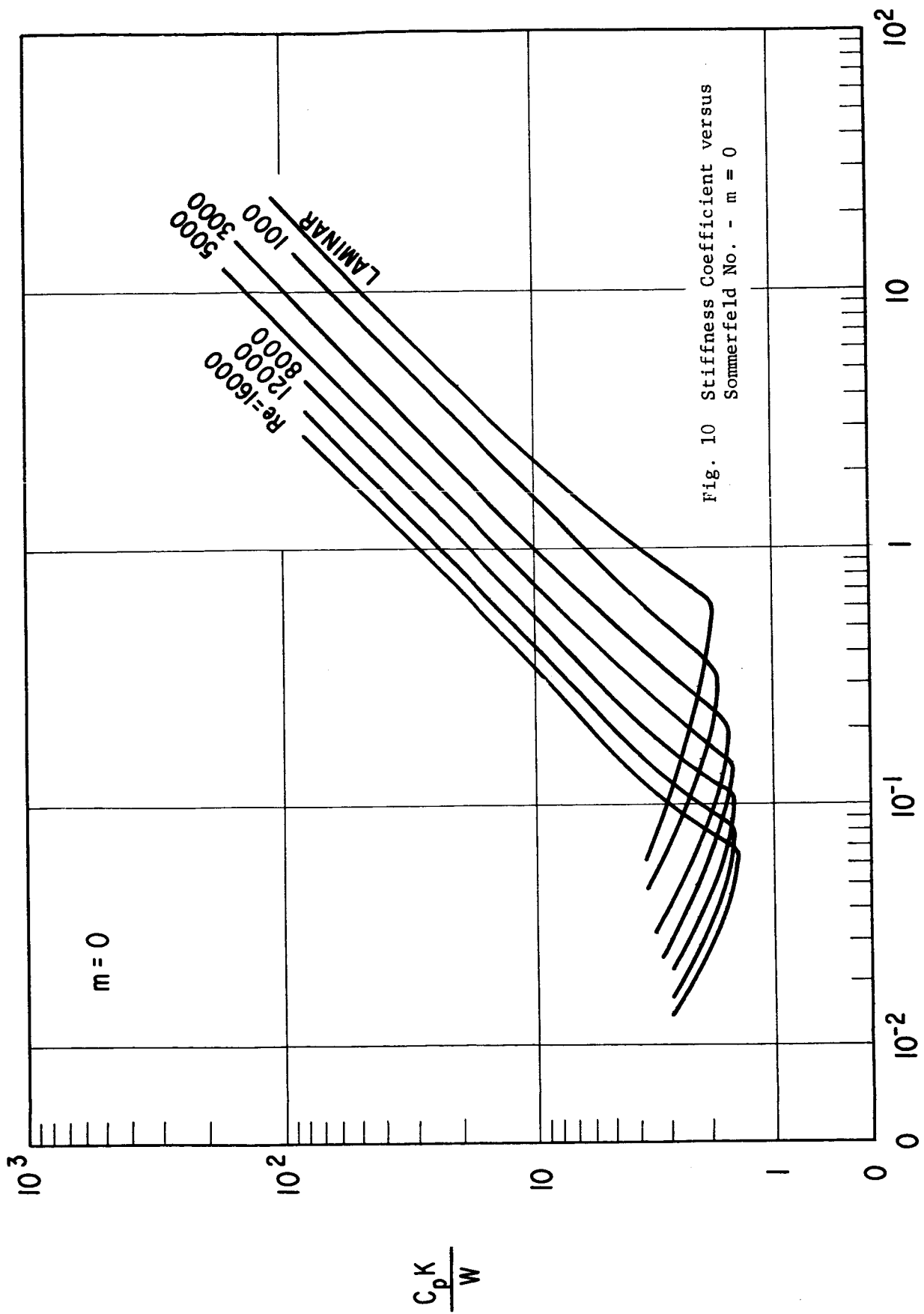


Fig. 9 Attitude Angle versus Eccentricity
for Single Pad
 $\rho = 80$
 $\theta_p = .55$



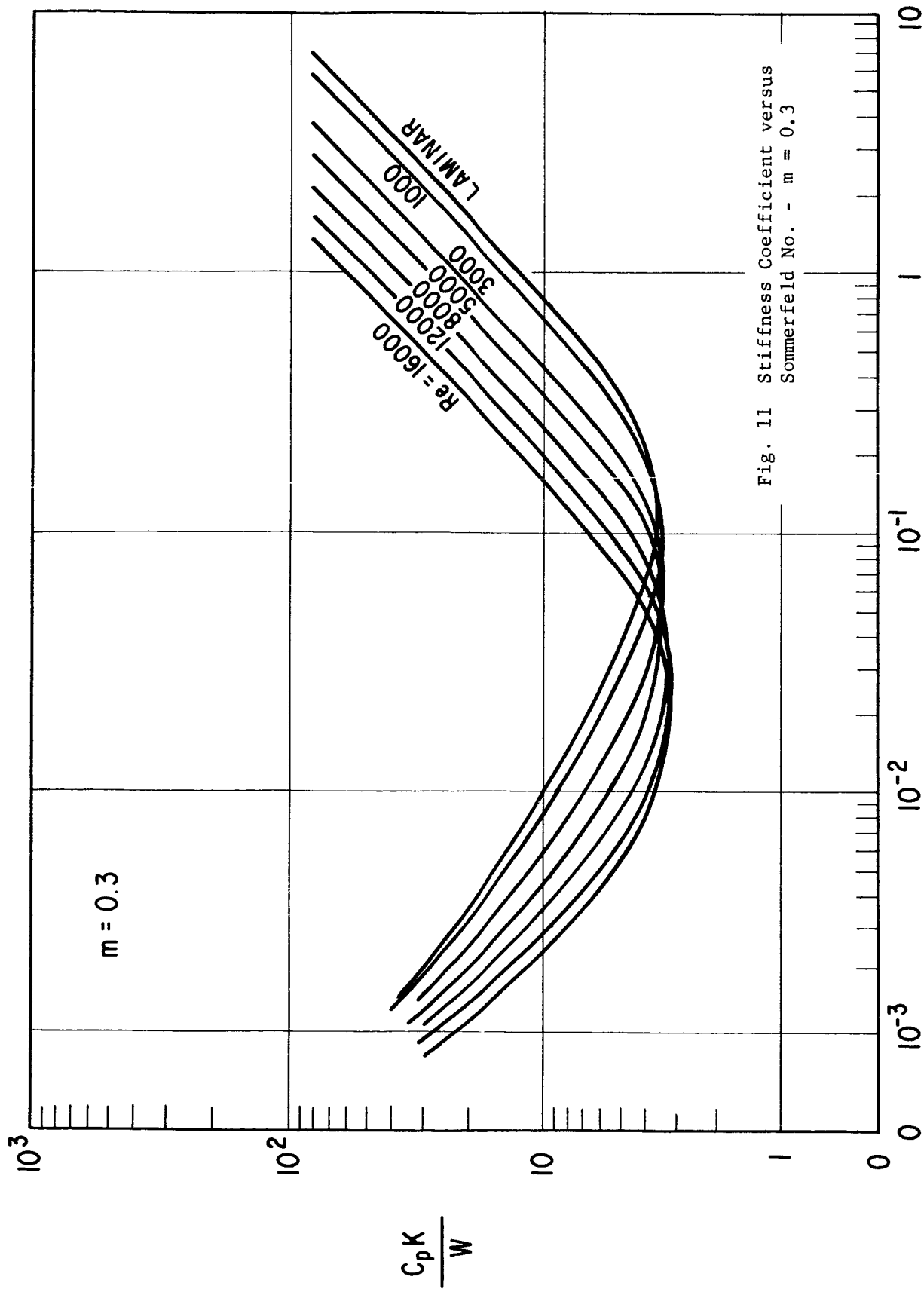


Fig. 11 Stiffness Coefficient versus Sommerfeld No. - $m = 0.3$

$$S = \frac{\mu_{NLD}}{W} \left(\frac{R}{C_p} \right)^2$$

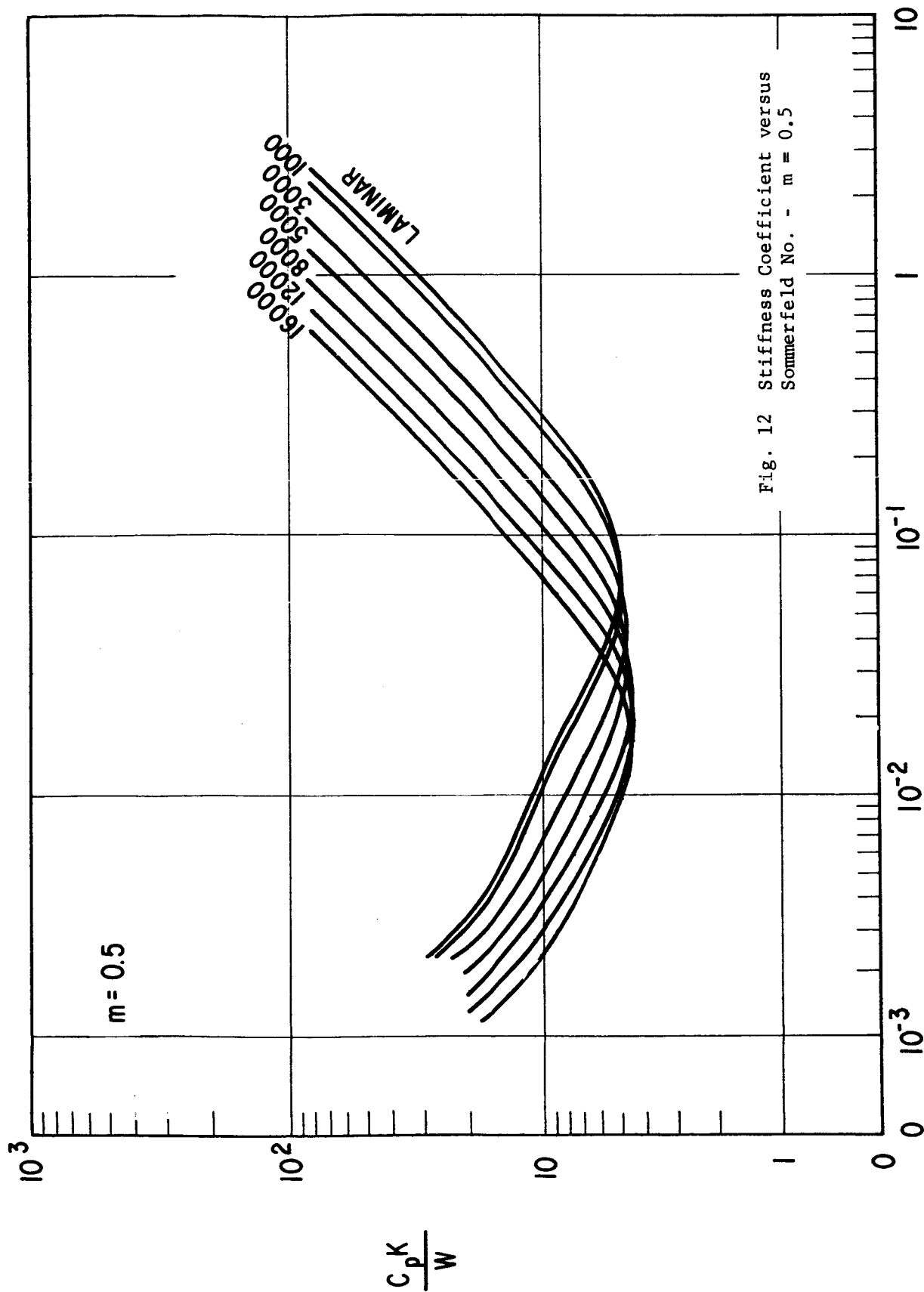


Fig. 12 Stiffness Coefficient versus Sommerfeld No. - $m = 0.5$

$$S = \frac{\mu_{NLD}}{W} \left(\frac{R}{C_p} \right)^2$$

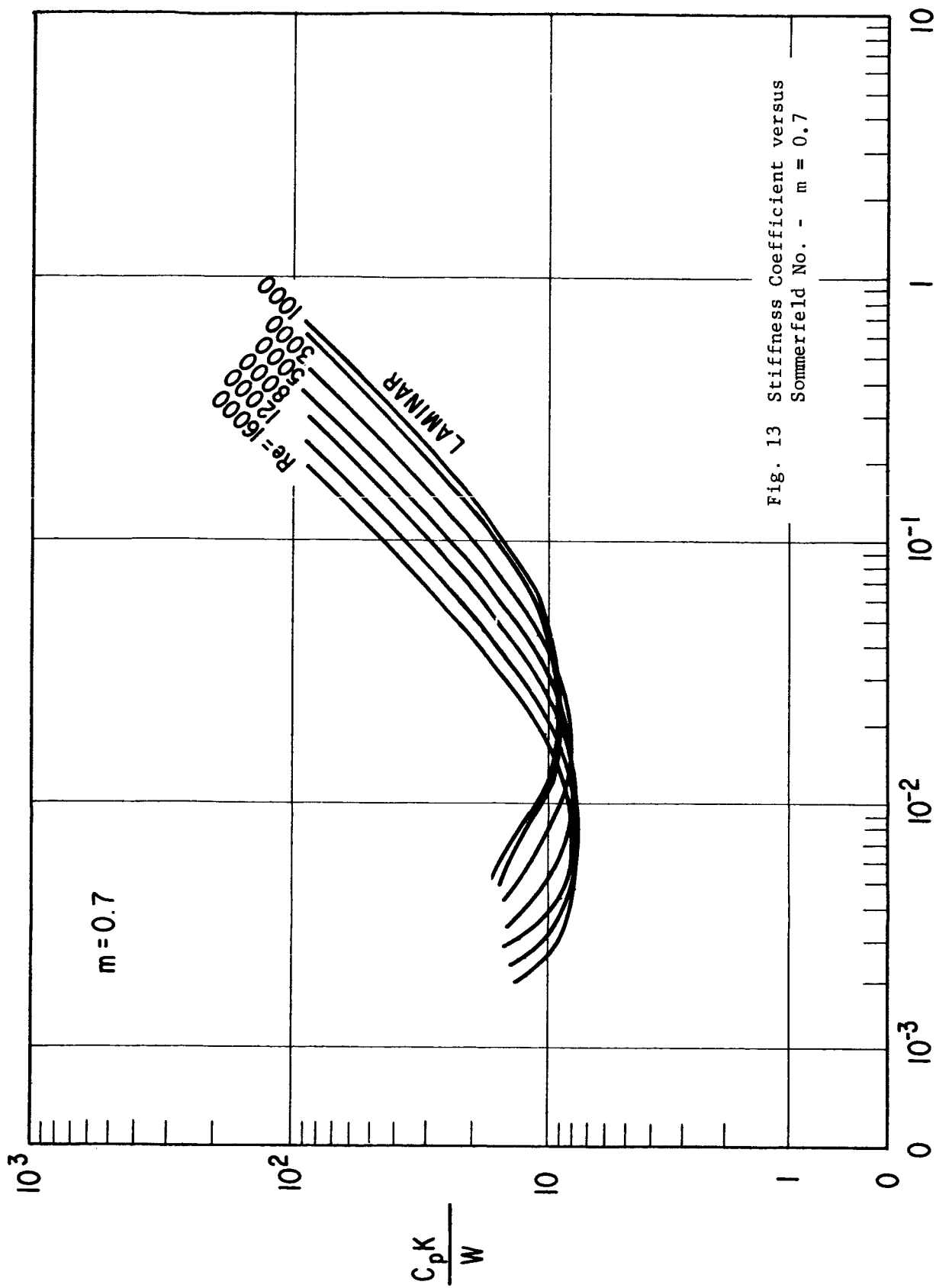


Fig. 13 Stiffness Coefficient versus
Sommerfeld No. - $m = 0.7$

$$S = \frac{\mu_{NLD} R^2}{W C_p}$$

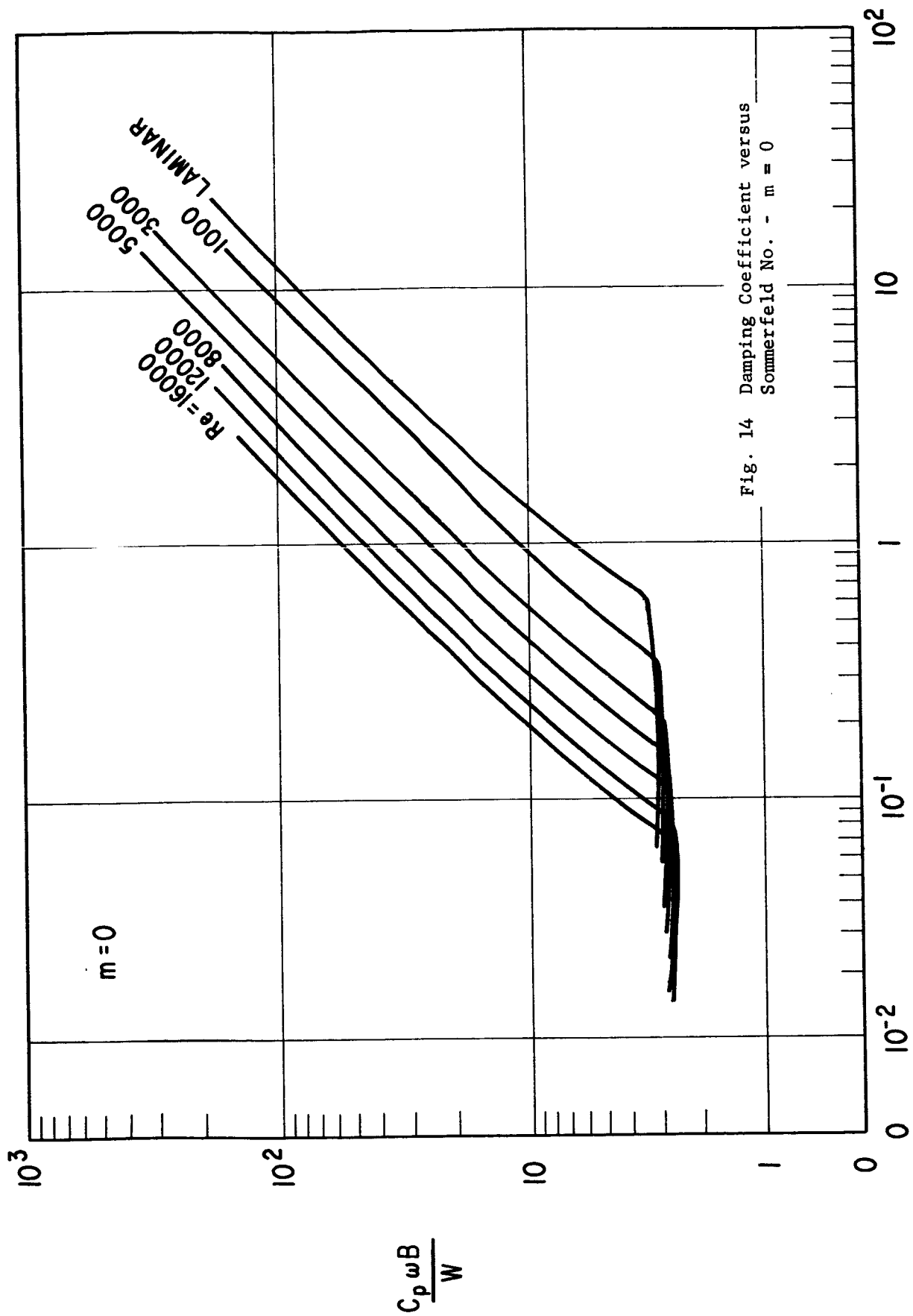
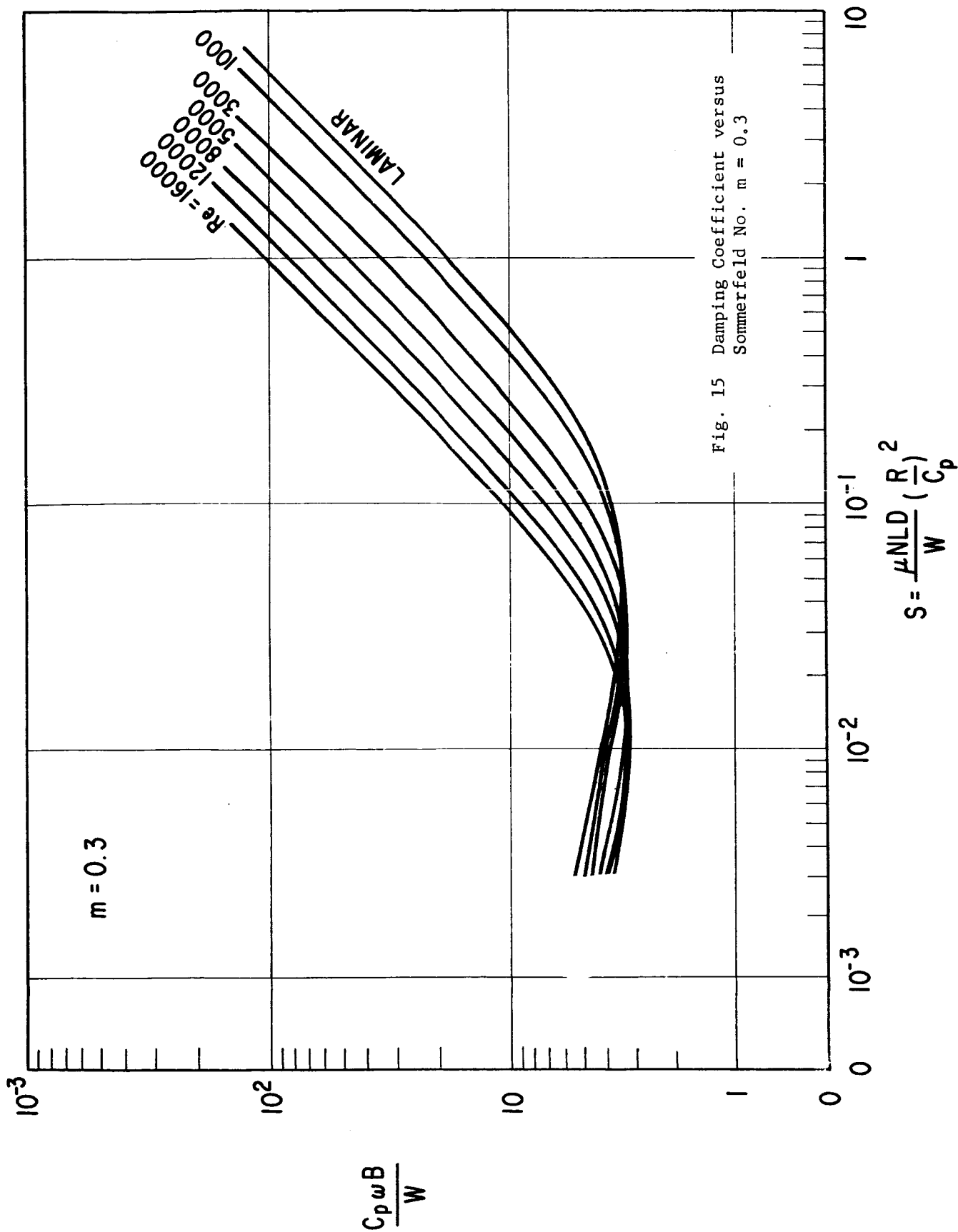
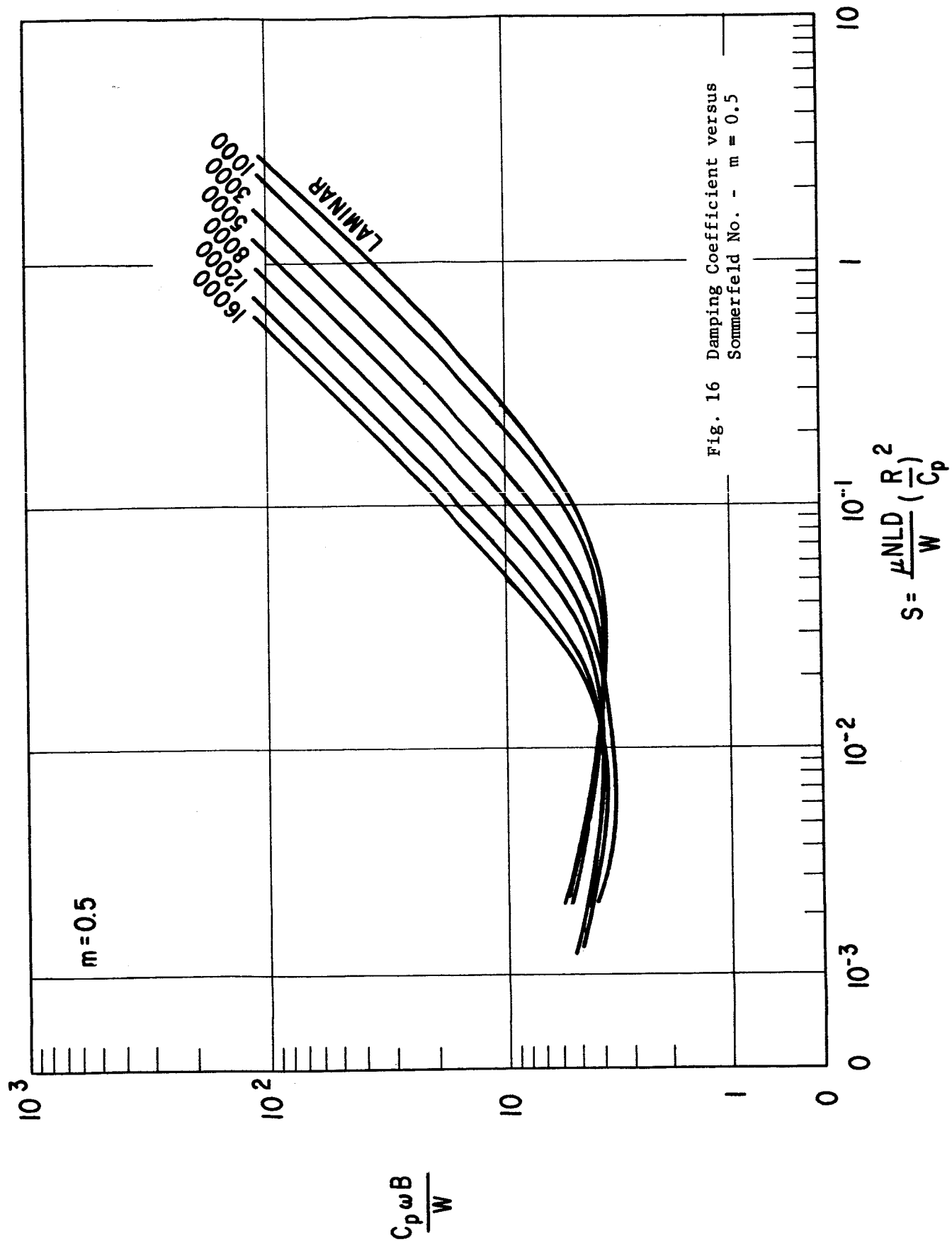
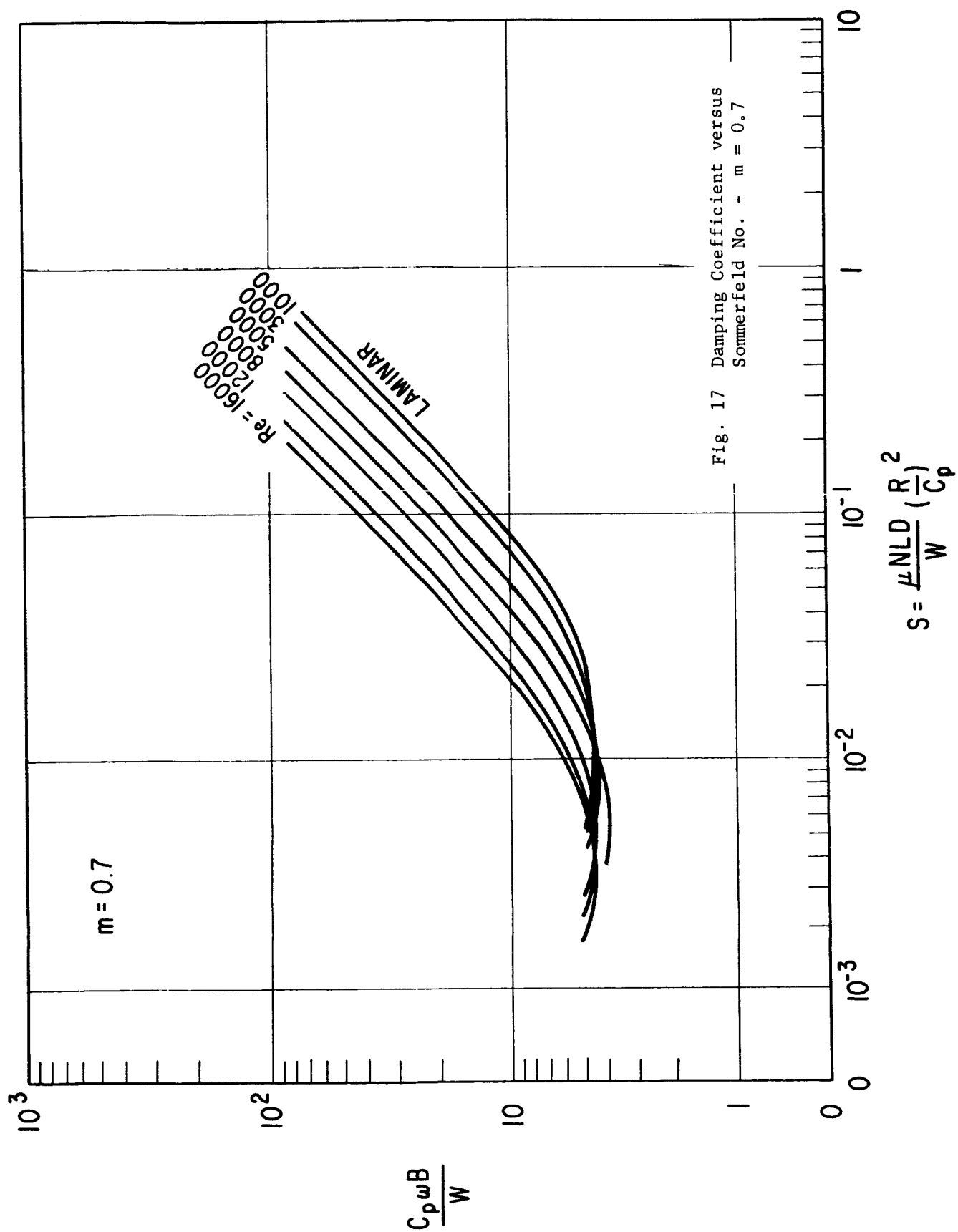


Fig. 14 Damping Coefficient versus Sommerfeld No. - $m = 0$







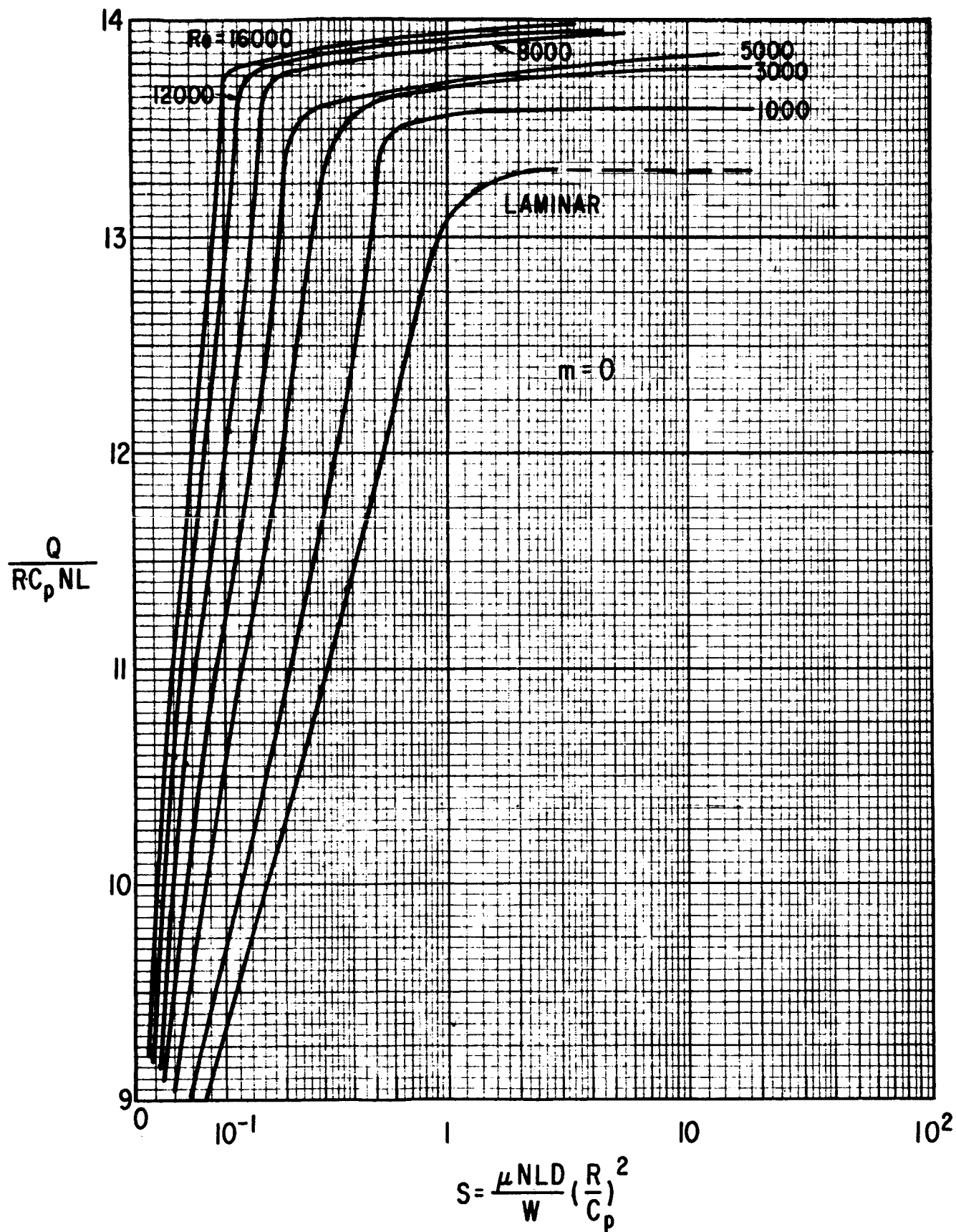


Fig. 18 Dimensionless Flow versus Sommerfeld No. - $m = 0$

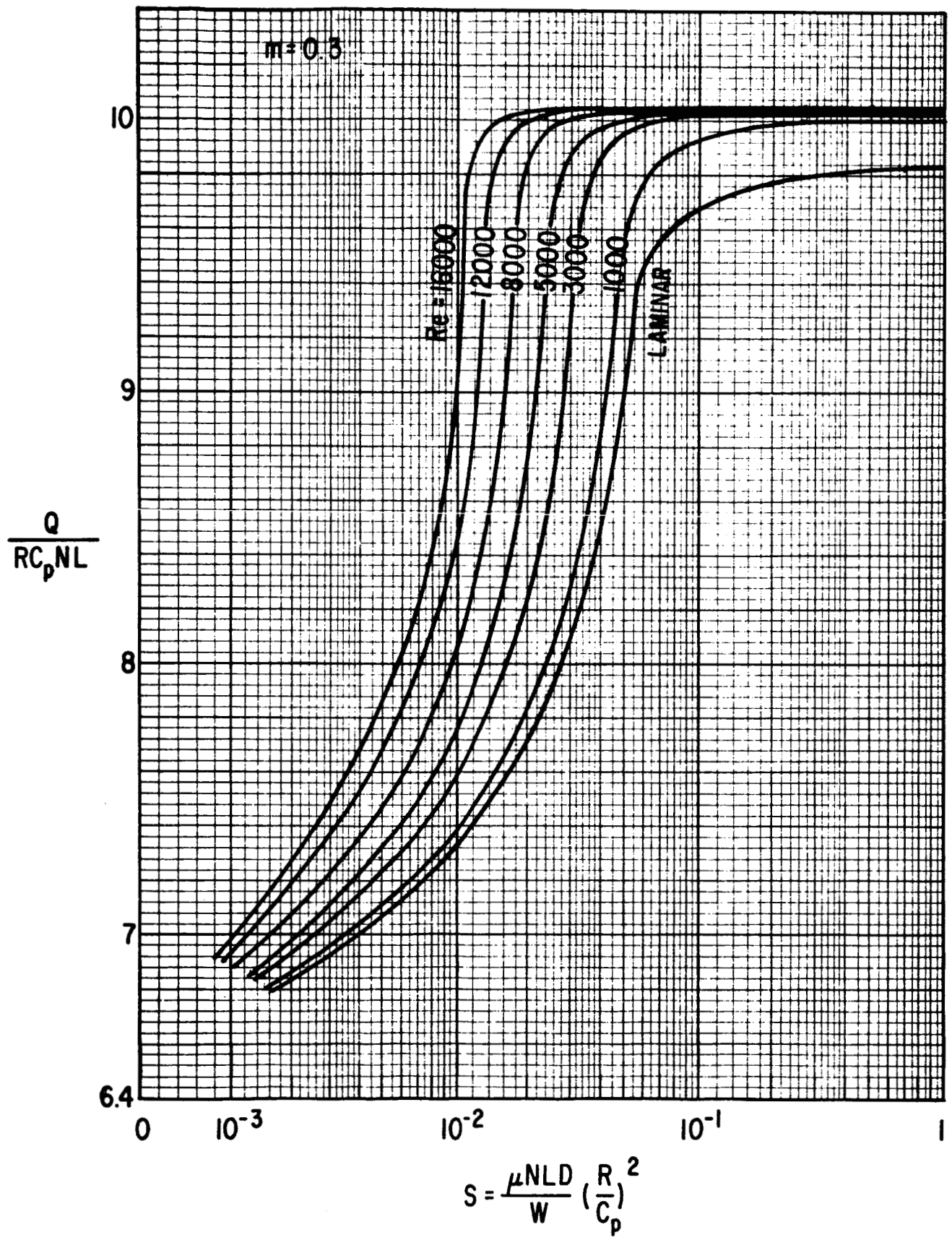


Fig. 19 Dimensionless Flow versus Sommerfeld No. - $m = 0.3$

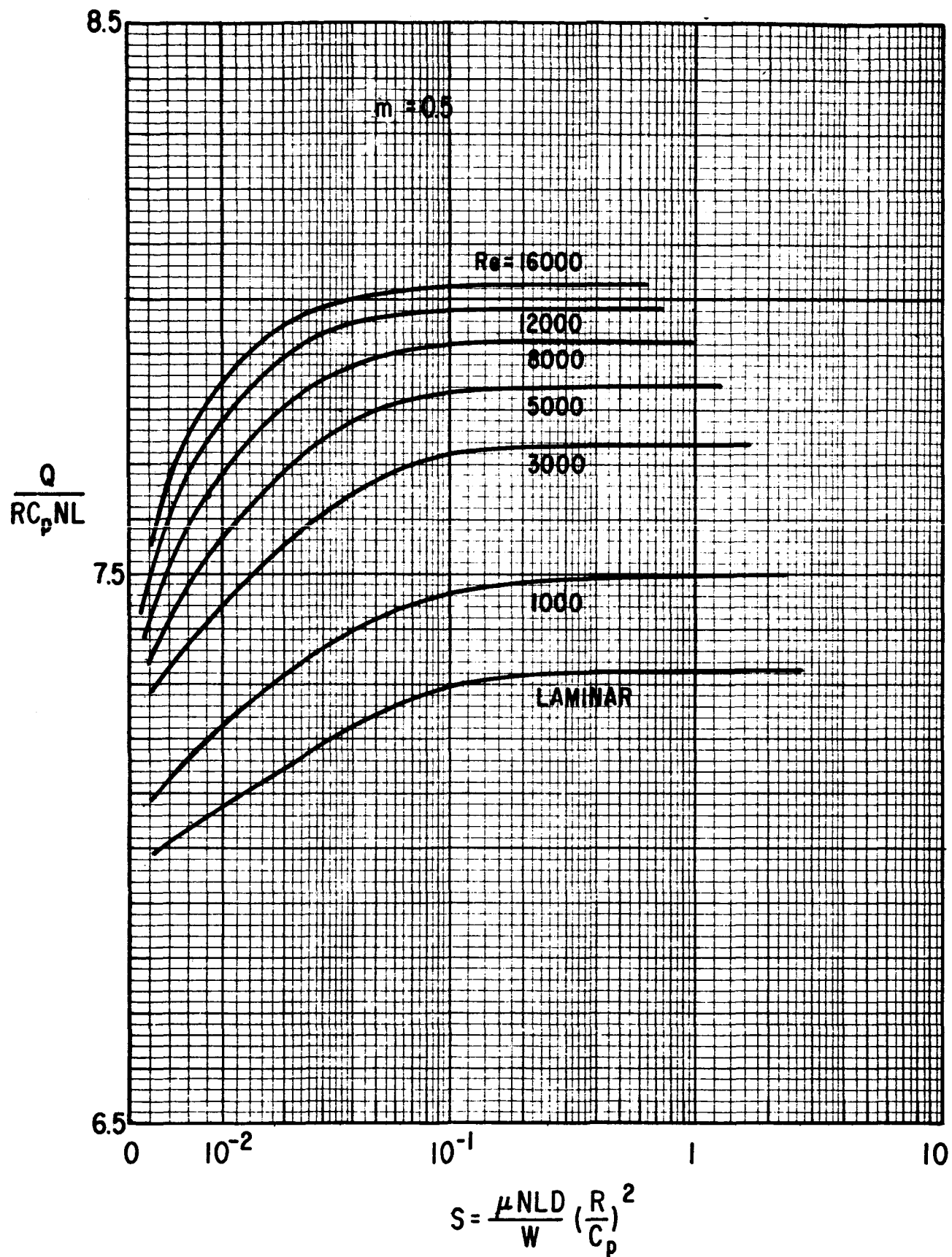


Fig. 20 Dimensionless Flow versus Sommerfeld - $m = 0.5$

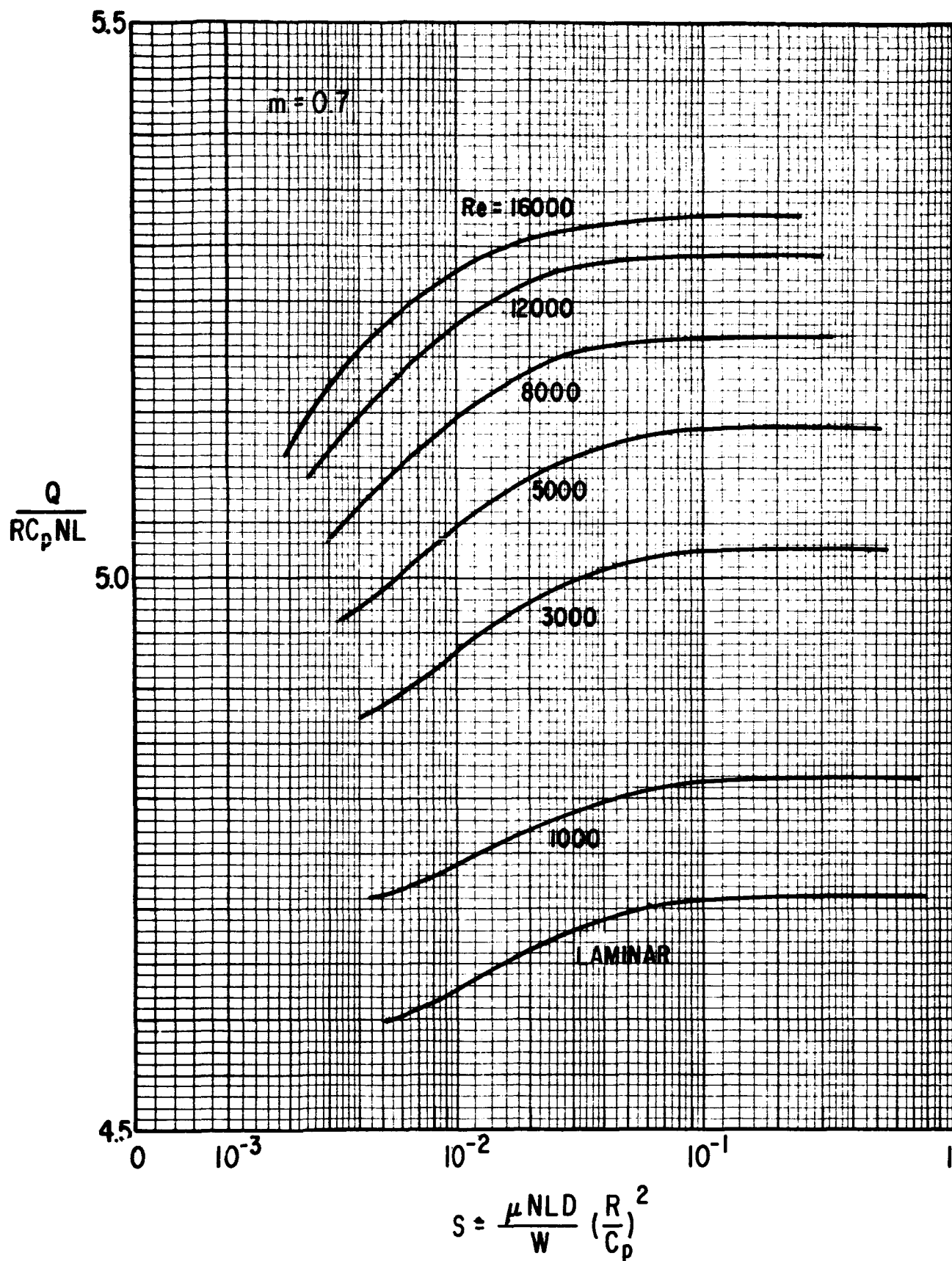


Fig. 21 Dimensionless Flow versus Sommerfeld No. - $m = 0.7$

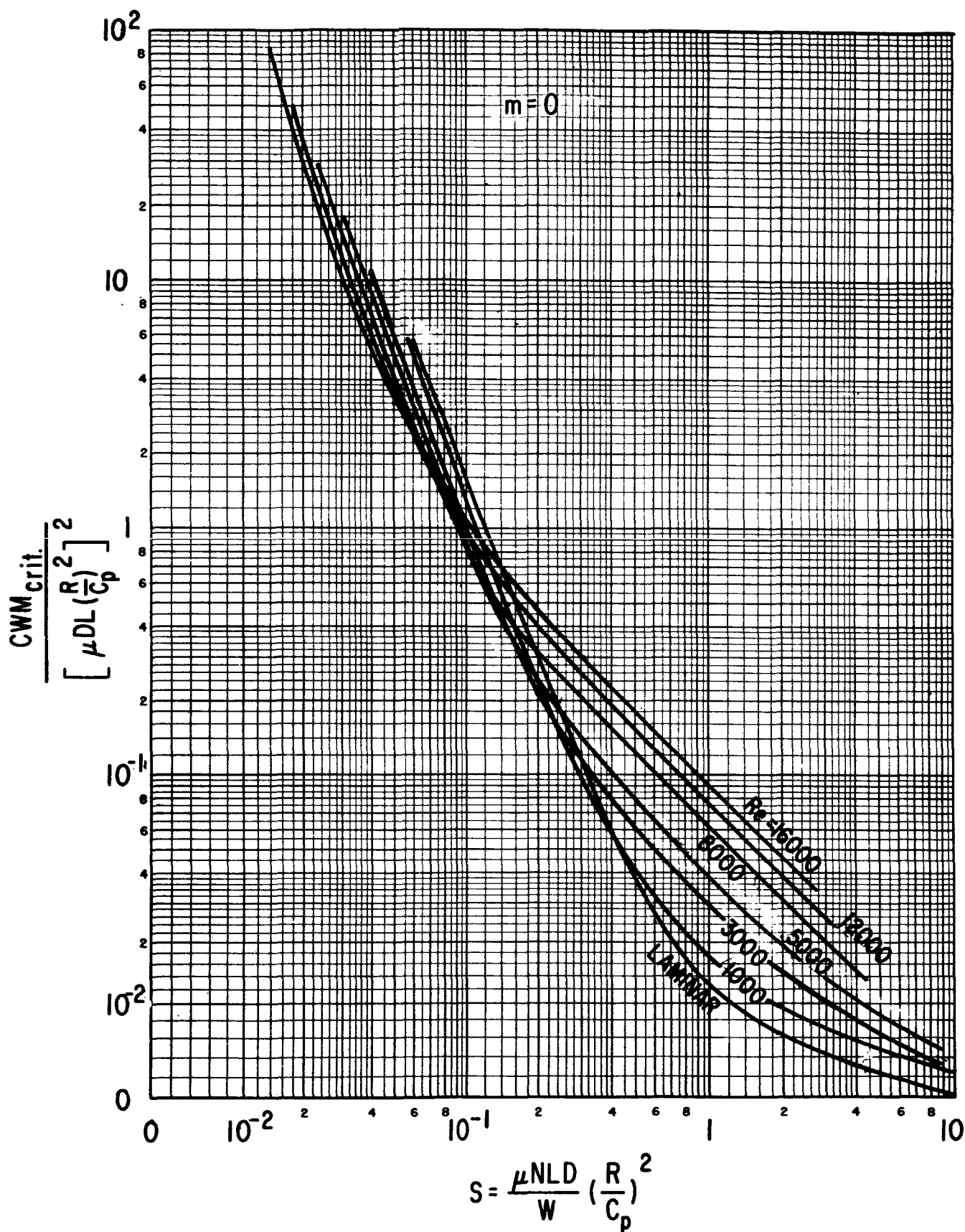


Fig. 22 Pad Critical Mass versus Sommerfeld No. - $m = 0$

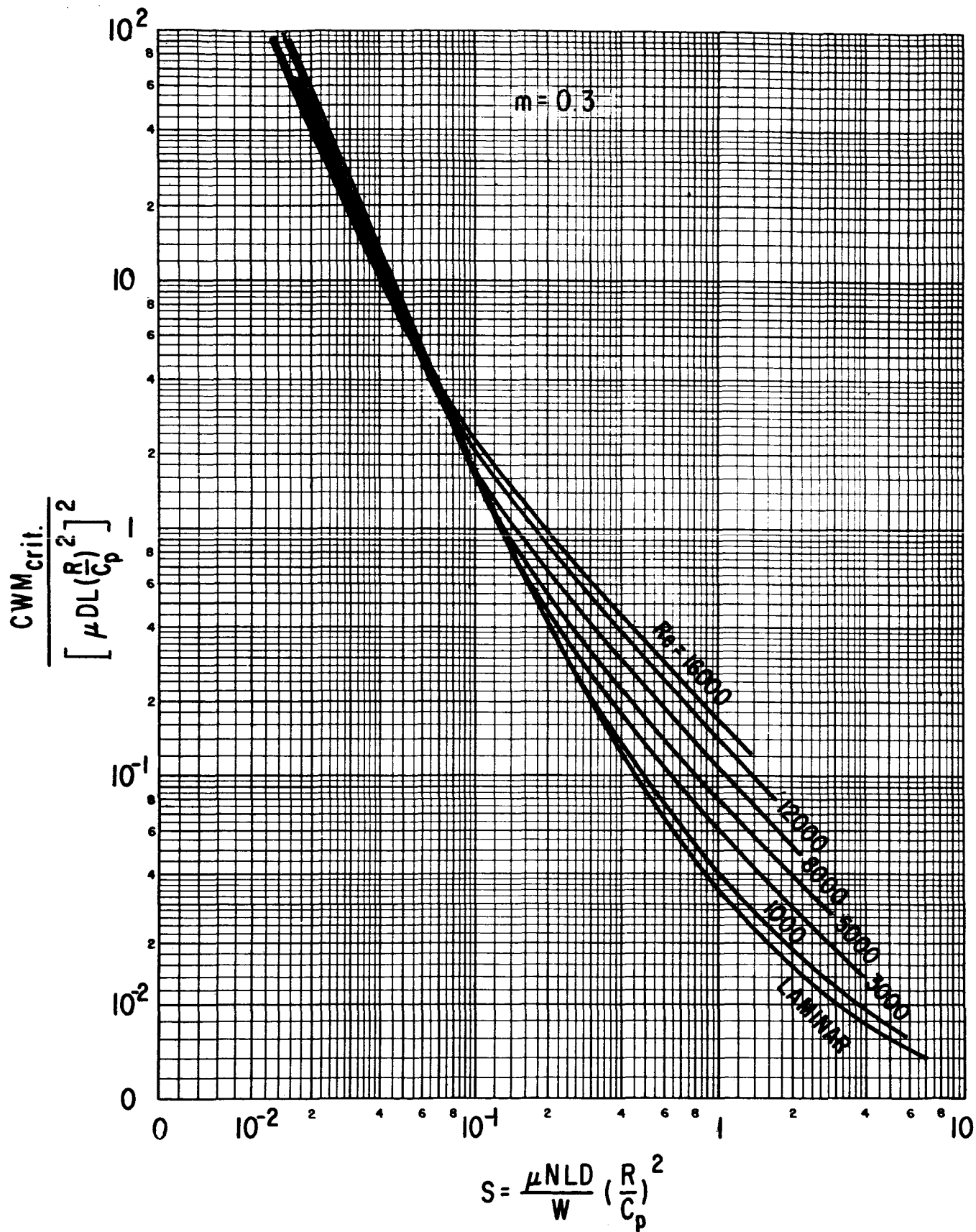
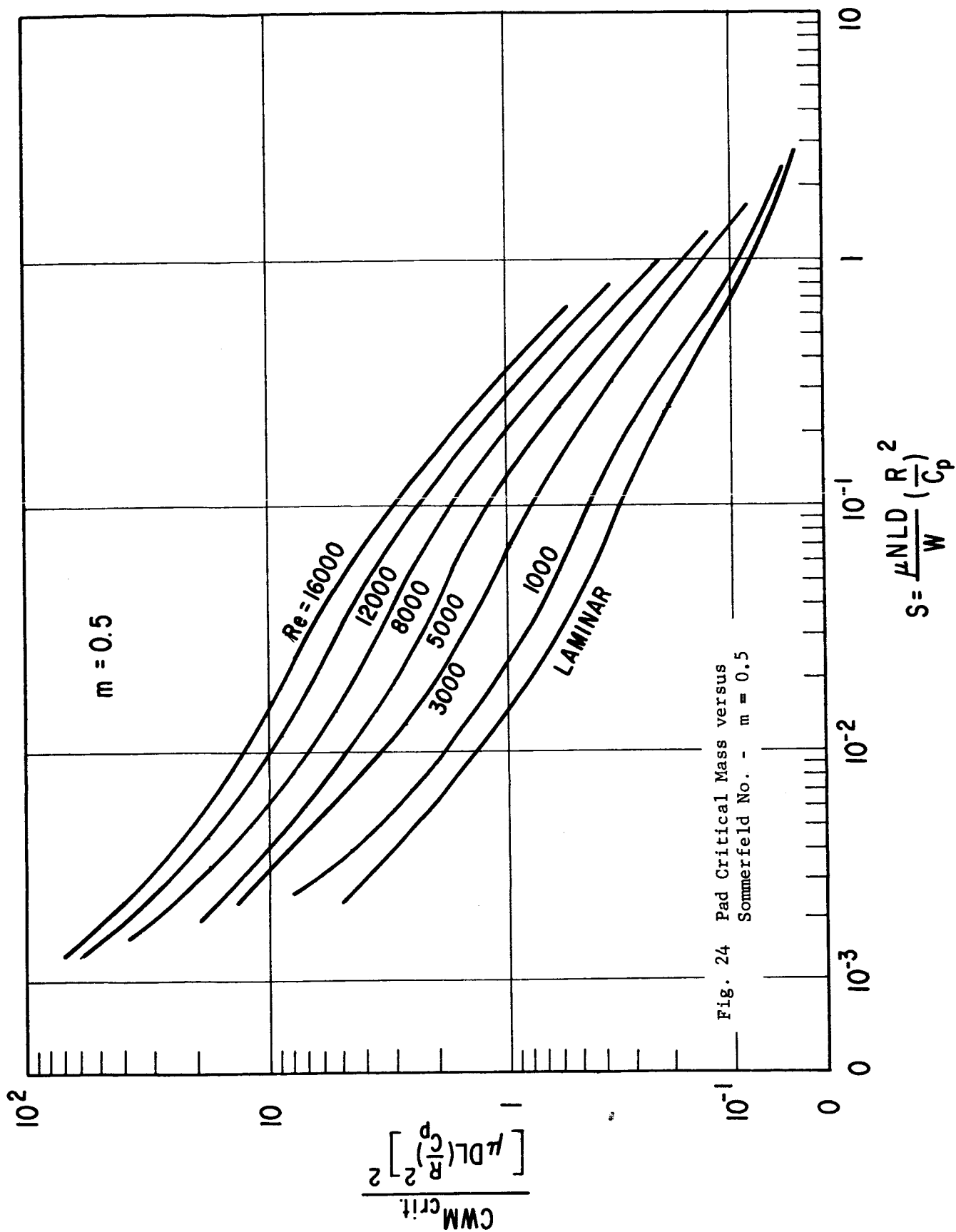
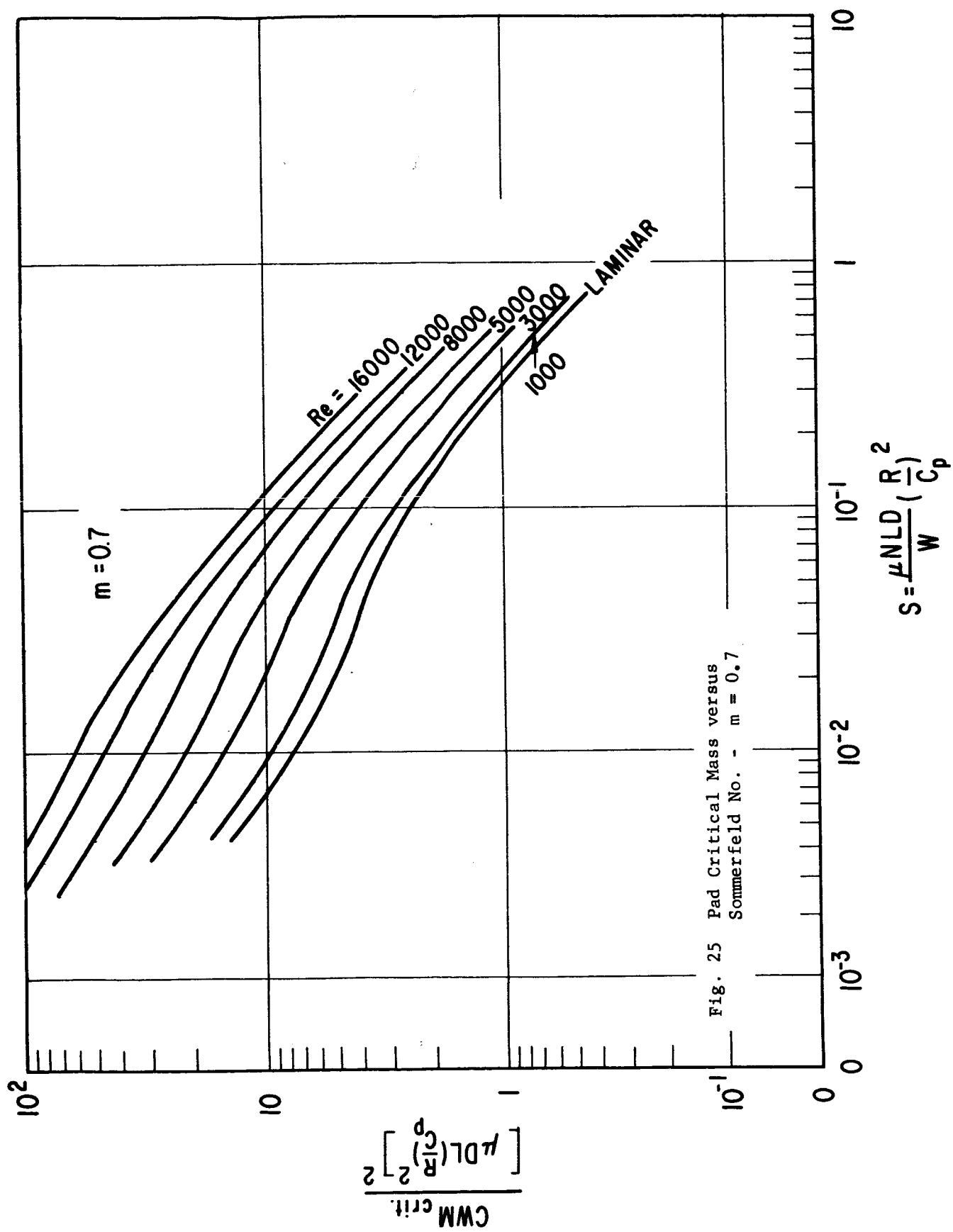


Fig. 23 Pad Critical Mass versus Sommerfeld No. - $m = 0.3$





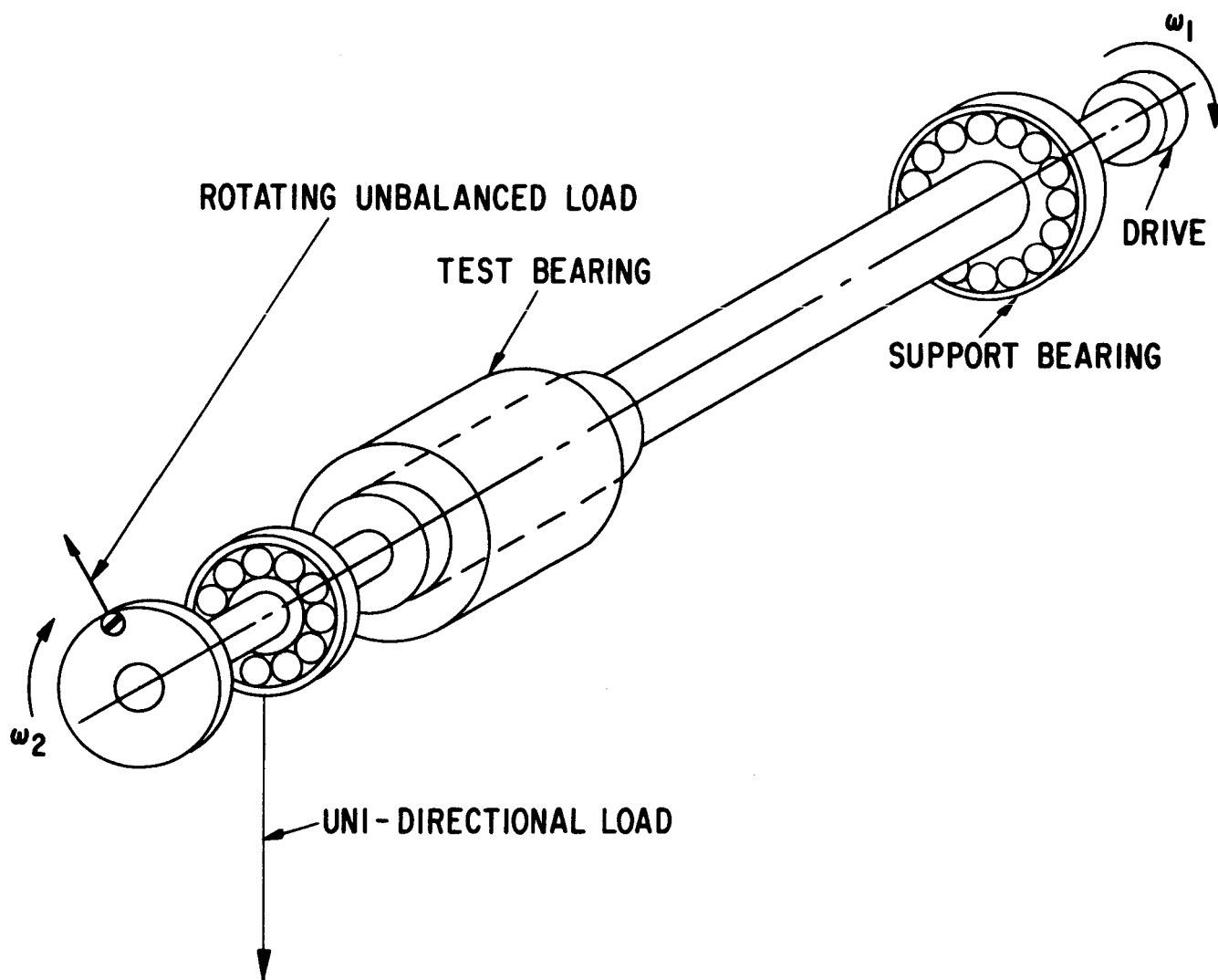


Fig. 26 Schematic of Apparatus Shaft and Bearing Assembly

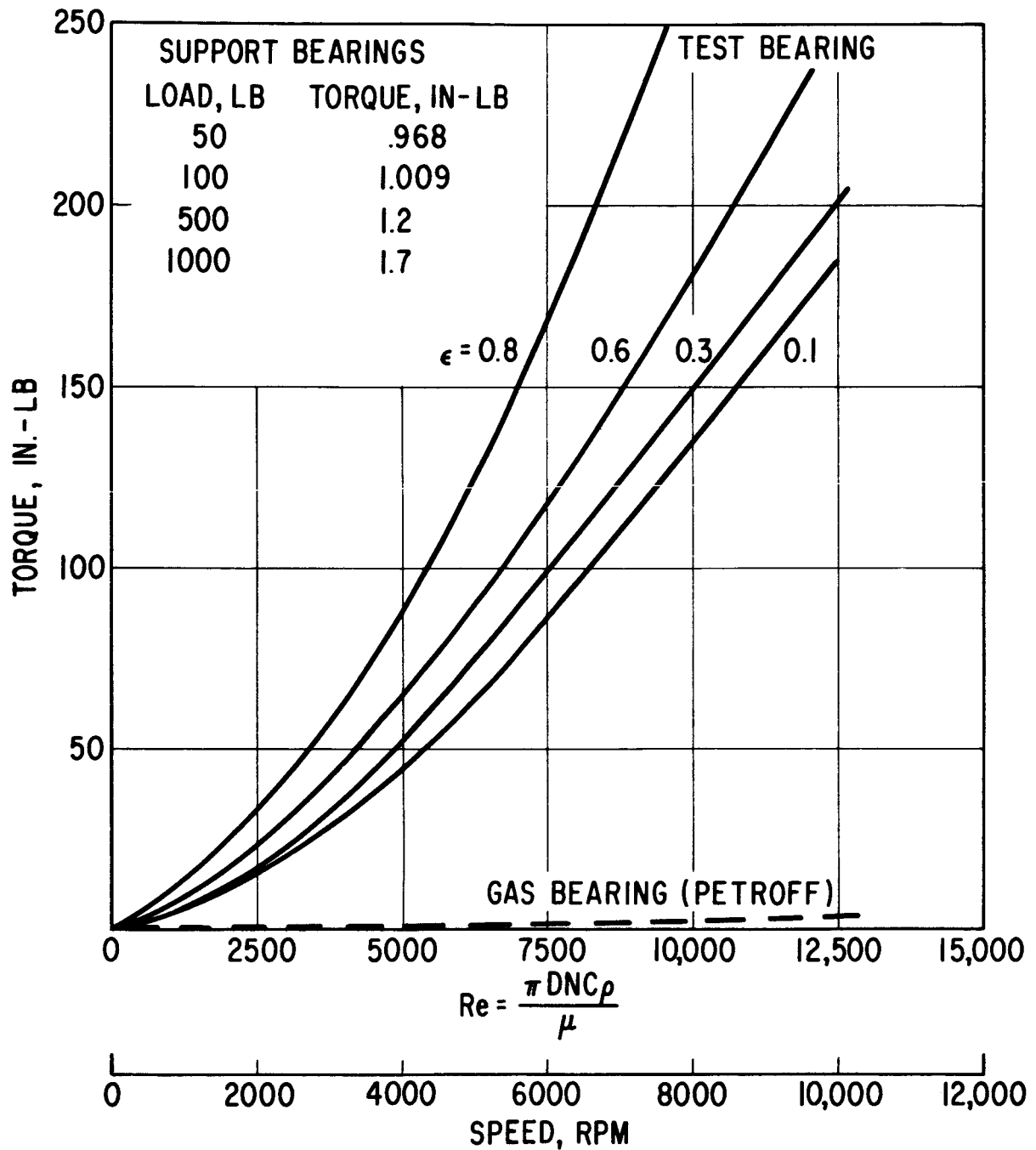


Fig. 27 Estimated Support and Test Bearing Torques

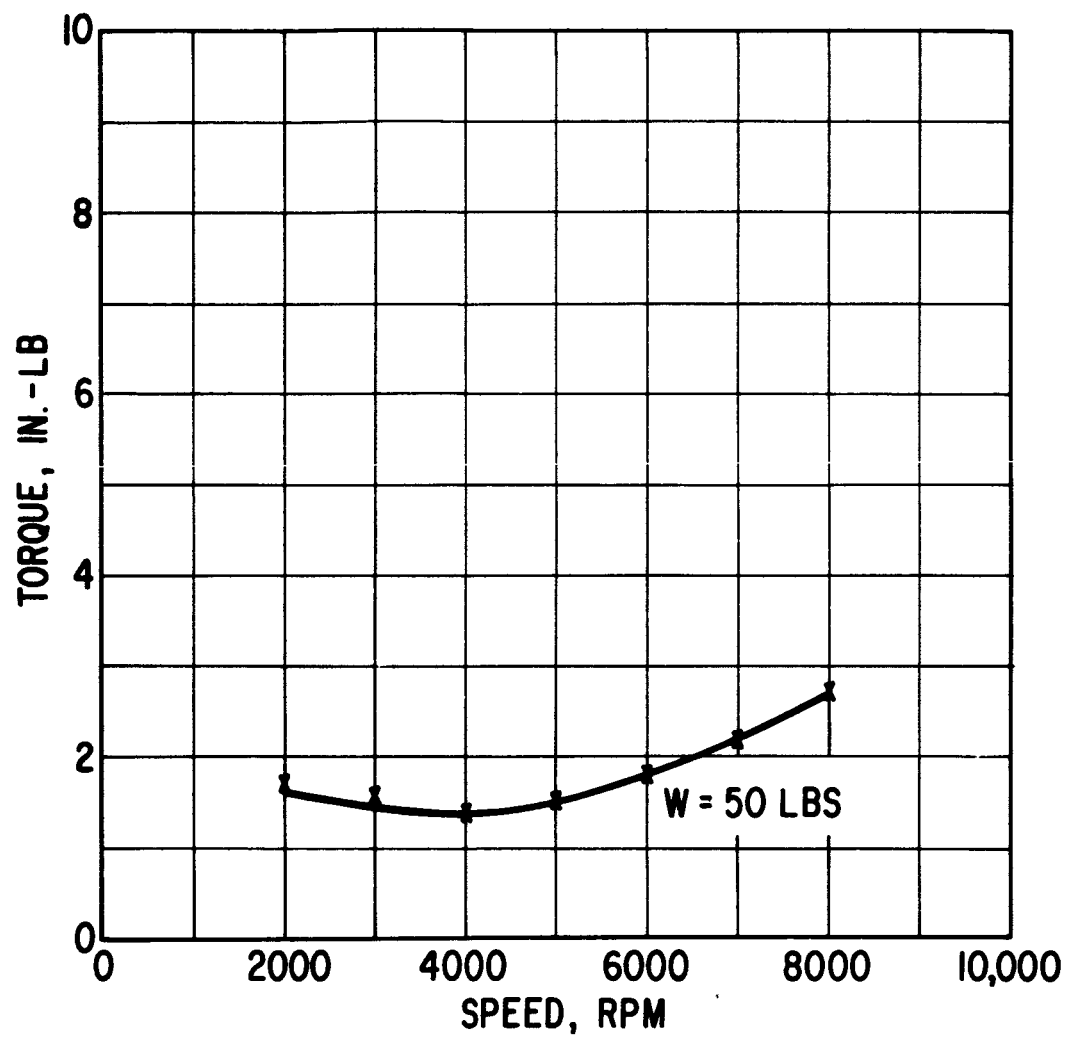


Fig. 28 Parasitic Torque Measurements
Correction for Gas Bearing Torque has been Made.

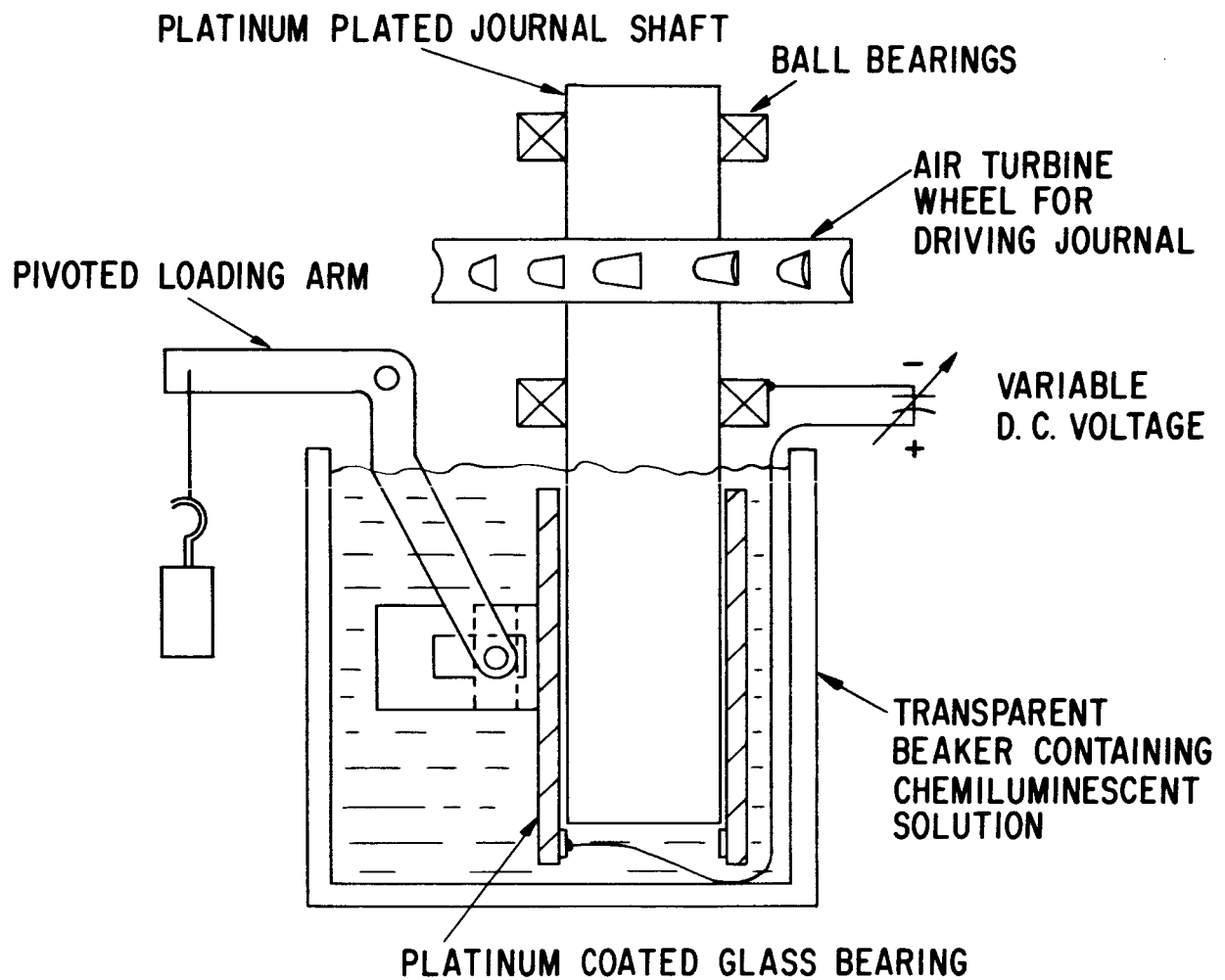


Fig. 29 Schematic of Electrochemiluminescent Bearing Flow Visualization Test Rig

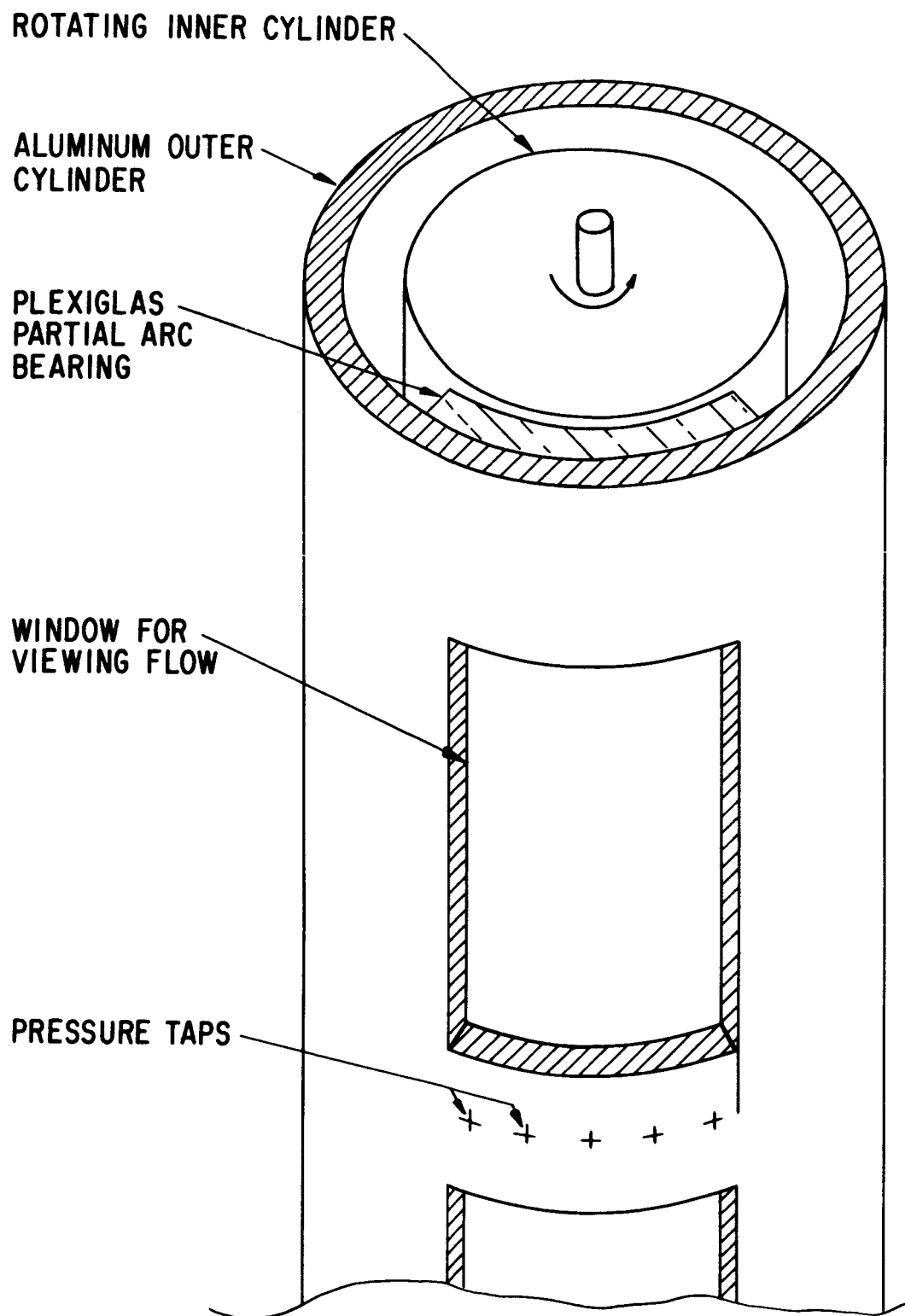


Fig. 30 Schematic of Partial Arc Bearing Test Rig